A multiwavelength exploration of the [C II]/IR ratio in *H*-ATLAS/GAMA galaxies out to $z = 0.2$

E. Ibar,[1]★ M. A. Lara-López,[2,3] R. Herrera-Camus,[4] R. Hopwood,[5] A. Bauer,[3]
R. J. Ivison,[6,7] M. J. Michałowski,[7] H. Dannerbauer,[8] P. van der Werf,[9]
D. Riechers,[10,11] N. Bourne,[7] M. Baes,[12] I. Valtchanov,[13] L. Dunne,[14,7] A. Verma,[15]
S. Brough,[3] A. Cooray,[16,10] G. De Zotti,[17,18] S. Dye,[19] S. Eales,[20] C. Furlanetto,[19,21]
S. Maddox,[7,14] M. Smith,[20] O. Steele,[22] D. Thomas[22] and E. Valiante[20]

Affiliations are listed at the end of the paper

ABSTRACT

We explore the behaviour of [C II] $\lambda157.74\,\mu m$ forbidden fine-structure line observed in a sample of 28 galaxies selected from $\sim 50\,deg^2$ of the *Herschel*-Astrophysical Terahertz Large Area Survey survey. The sample is restricted to galaxies with flux densities higher than $S_{160\,\mu m} > 150\,mJy$ and optical spectra from the Galaxy and Mass Assembly survey at $0.02 < z < 0.2$. Far-IR spectra centred on this redshifted line were taken with the Photodetector Array Camera and Spectrometer instrument on-board the *Herschel Space Observatory*. The galaxies span $10 < \log(L_{IR}/L_\odot) < 12$ (where $L_{IR} \equiv L_{IR}[8-1000\,\mu m]$) and $7.3 < \log(L_{[C II]}/L_\odot) < 9.3$, covering a variety of optical galaxy morphologies. The sample exhibits the so-called [C II] deficit at high-IR luminosities, i.e. $L_{[C II]}/L_{IR}$ (hereafter [C II]/IR) decreases at high L_{IR}. We find significant differences between those galaxies presenting [C II]/IR $>2.5 \times 10^{-3}$ with respect to those showing lower ratios. In particular, those with high ratios tend to have: (1) $L_{IR} < 10^{11}\,L_\odot$; (2) cold dust temperatures, $T_d < 30\,K$; (3) disc-like morphologies in *r*-band images; (4) a *Wide-field Infrared Survey Explorer* colour $0.5 \lesssim S_{12\,\mu m}/S_{22\,\mu m} \lesssim 1.0$; (5) low surface brightness $\Sigma_{IR} \approx 10^{8-9}\,L_\odot\,kpc^{-2}$, (6) and specific star formation rates of sSFR $\approx 0.05-3\,Gyr^{-1}$. We suggest that the strength of the far-UV radiation fields ($\langle G_O \rangle$) is main parameter responsible for controlling the [C II]/IR ratio. It is possible that relatively high $\langle G_O \rangle$ creates a positively charged dust grain distribution, impeding an efficient photoelectric extraction of electrons from these grains to then collisionally excite carbon atoms. Within the brighter IR population, $11 < \log(L_{IR}/L_\odot) < 12$, the low [C II]/IR ratio is unlikely to be modified by [C II] self-absorption or controlled by the presence of a moderately luminous AGN (identified via the BPT diagram).

Key words: ISM: evolution – ISM: lines and bands – galaxies: starburst – infrared: ISM.

1 INTRODUCTION

Understanding the chemical and physical evolution of a galaxy is far from trivial. Newly born stars consume and process the available gas, whilst heating the interstellar medium (ISM), and supernovae enrich the environment with heavy elements, contributing to potentially complex feedback processes. A good description of ISM physics under the influence of stellar radiation fields was achieved using photo-dissociation region (PDR) modelling (e.g. Tielens &

Hollenbach 1985). These models can explain the origin of most of the dense ISM emission from star-forming galaxies, including the major cooling fine-structure lines of carbon/nitrogen/oxygen (C/N/O) and the underlying infrared (IR) continuum emission produced by interstellar dust.

At IR wavelengths, the most prominent emission line is [C II] $\lambda157.74\,\mu m$ ($^2P_{3/2} \rightarrow ^2P_{1/2}$; $E_{ul}/k = 92\,K$), which carries ~ 0.1–1 per cent of the bolometric power emitted by star-forming galaxies (Stacey et al. 1991, 2010), with a [C II] flux typically 1000 times that of CO ($J = 1$–0) at 115 GHz. The low ionization potential, 11.26 eV, makes [C II] a key participant in cooling the warm and diffuse media, converting it into cold and dense clouds

that can then collapse to form stars (Dalgarno & McCray 1972). As a fine-structure line, [C II] is an excellent tracer of all the different stages of evolution of the ISM: it can be excited by collisions with electrons in the warm ionized medium; H I in the warm or cold diffuse media; and H₂ in the warm and dense molecular gas. Its intensity is sensitive to the column density, the volume density and the kinetic temperature of the ISM (Pineda et al. 2013).

In the plane of the Milky Way, Pineda et al. (2013) show that the [C II] line emission emerges predominantly at Galactocentric distances between 4 and 10 kpc. Considering a scaleheight for the Galaxy, Pineda, Langer & Goldsmith (2014) finds that the ISM components that contribute to the [C II] luminosity of the Galaxy have roughly comparable contributions: 30 per cent comes from dense PDRs, ~20 per cent from ionized gas, ~25 per cent from diffuse atomic gas and ~25 per cent from CO-dark H₂ (at the surface of molecular clouds where carbon is not in the form of CO). In the local spiral galaxy M 33, Kramer et al. (2013) suggest that the [C II] emission related to neutral gas corresponds to ~15 per cent of the total within 2 kpc from the galaxy centre, while this percentage seems to increment up to ~40 ± 20 per cent in the outer part of the disc (between 2 and 7 kpc).

In distant galaxies, strong observational limitations impede a detailed characterization of the different phases of the ISM. Typically detected in a single telescope beam, the ISM phases are all mixed together, hence [C II] line detections relate to averaged quantities of an ensemble of individual PDRs, ionized regions, etc. Madden et al. (1993) suggest that ~75 per cent of the [C II] emission from the spiral galaxy NGC 6946 originates from cold neutral hydrogen clouds, and ≲40 per cent from the diffuse galaxy disc (Contursi et al. 2002). On the other hand, averaged ISM properties of luminous and ultraluminous IR galaxies (LIRGs and ULIRGs) are found to vary considerably with respect to those observed in the Milky Way. LIRGs/ULIRGs present much higher star formation rates (SFRs) and evidence much larger amounts of ionized gas – up to 50 per cent of the total (e.g. Malhotra et al. 2001). The rest of their [C II] luminosity is expected to come from dense PDR-related ISM (e.g. Negishi et al. 2001). At the other extreme, Cormier et al. (2012) estimate that the low metallicity dwarf star-forming galaxy Haro 11 produces only 10 per cent of its [C II] emission in PDRs, probably because radiation fields penetrate deep into the ISM components.

The examples shown above clearly evidence the intricate decomposition of the [C II] emission into the different ISM phases. Great effort has been dedicated to find [C II] correlations with various galaxy properties. Previous studies have shown that the integrated [C II] line strength depends on the polycyclic aromatic hydrocarbon (PAH) emission lines (e.g. Bakes & Tielens 1994), IR colour (Malhotra et al. 2001), the degree of active galactic nuclei (AGN; e.g. Stacey et al. 2010) activity, among other various correlations. Those with powerful AGN show fainter [C II] than pure star-forming galaxies, at fixed L_{IR} (Negishi et al. 2001; Sargsyan et al. 2012). [C II] has also been used for diagnostic purposes in galaxies at cosmological distances (e.g. Ivison et al. 2010; Valtchanov et al. 2011; George et al. 2013) and has sometimes betrayed a galaxy's redshift (e.g. Swinbank et al. 2012; George et al. 2013). Indeed, [C II] is a potentially unrivalled tracer of the total gas mass or the SFR or the dynamics in the most distant galaxies (Maiolino et al. 2005; De Breuck et al. 2014; De Looze et al. 2014; Herrera-Camus et al. 2015).

Early observations of local star-forming galaxies with the Kuiper Airborne Observatory (Stacey et al. 1991) and the *Infrared Space Observatory* (Malhotra et al. 1997) showed that [C II]/IR is roughly constant at $1–3 \times 10^{-3}$ (with a factor of 3 of scatter) for

$L_{IR} < 10^{11}$ L$_\odot$ galaxies (it is higher in low-metallicity environments – Madden 2000; Rubin et al. 2009), although it drops rapidly at higher L_{IR}. This behaviour is usually referred to as the '[C II] deficit'. [C II]/IR also correlates strongly with 60 μm/100 μm colour (a proxy for dust temperature, e.g. Díaz-Santos et al. 2013) and the IR/*B*-band luminosity ratio, L_{IR}/L_B (Malhotra et al. 2001). Various explanations for the [C II] deficit have been offered: (1) in high radiation fields, photoionization of dust grains might saturate, hence the energy of their ejected photoelectrons is reduced, reducing also the gas heating (Luhman et al. 2003); (2) the deficit is due to an increase in the collisional de-excitation of the [C II] transition due to an increase in gas density (Negishi et al. 2001); (3) a significant fraction of the IR emission may arise from dust absorption of photons from old stellar populations which are not related directly to PDRs (e.g. Rowan-Robinson et al. 2010); (4) a significant portion of the IR emission could emanate from 'dust-bounded' structures within photoionized gas regions, but the [C II] line does not (Luhman et al. 2003; Abel et al. 2009); (5) the [C II] line may be self-absorbed or optically thick (e.g. NGC 6334 – Boreiko & Betz 1995) in highly embedded regions (Fischer et al. 2010, see also Gerin et al. 2015)), or (6) the level of IR emission in the most IR-luminous objects may be boosted by AGN activity (Curran 2009; Sargsyan et al. 2012).

Recent evidence, based on observations of local star-forming galaxies with the *Herschel Space Observatory*[1] (Pilbratt et al. 2010), points to different modes of star formation driven by the star-formation efficiency, L_{IR}/M_{H_2} (e.g. Young et al. 1986), regardless of the origin of the ionized or neutral phase of the ISM (Graciá-Carpio et al. 2011). Graciá-Carpio et al. find that $L_{IR}/M_{H_2} \gtrsim 100$ L$_\odot$ M$_\odot^{-1}$ marks a point at which the average properties of the neutral and ionized gas are significantly different. Using a sample of powerful star-forming galaxies they propose a scenario in which highly compressed, more efficient star formation, creates largely enhanced ionization parameters that manifest themselves in lower line to continuum ratios. This value of L_{IR}/M_{H_2} is closely related to that at which Genzel et al. (2010) and Daddi et al. (2010) claim a transition to a more efficient star formation mode, above the so-called 'main sequence' for star-forming galaxies (Elbaz et al. 2011).

Herschel was able to observe [C II] line emission from many local galaxies – a legacy that will last into the era of SPICA (the Space Infrared Telescope for Cosmology and Astrophysics – Nakagawa, Matsuhara & Kawakatsu 2012). Comprehensive analyses of these observations are mandatory if we are to interpret ground-based observations of [C II] towards high-redshift galaxies, e.g. with the Atacama Large Millimeter Array, where the [C II] line is shifted into accessible atmospheric windows (e.g. Maiolino et al. 2005, 2009; Walter et al. 2009; De Breuck et al. 2011, 2014; Riechers et al. 2013, 2014). Indeed, recent studies of luminous, high-redshift galaxies have revealed a [C II] behaviour which contrasts with that seen locally. Instead of looking like powerful ULIRGs – at the same luminosity – they exhibit striking similarities in terms of [C II]/IR ratios to normal local star-forming galaxies (Hailey-Dunsheath et al. 2010; Ivison et al. 2010; Stacey et al. 2010; Valtchanov et al. 2011).

In this paper, we present *Herschel* Photodetector Array Camera and Spectrometer (PACS; Poglitsch et al. 2010) Integral Field Unit (IFU) detections of a sample of dusty galaxies. We populate the $L_{[C II]}$ versus L_{IR} diagram with galaxies that lie at distances between 90 Mpc ($z \sim 0.02$) and 1000 Mpc ($z \sim 0.2$). This study therefore

---

[1] *Herschel* is an ESA space observatory with science instruments provided by European-led Principal Investigator consortia and with important participation from NASA.

bridges the gap between local galaxies and the growing body of data acquired for galaxies at high redshift. Our study performs a uniquely wide and detailed parameter space exploration that perfectly complements recent *Herschel* studies at low and intermediate redshifts, e.g. the *Herschel* ULIRG Survey (Farrah et al. 2013) and the Great Observatories All-sky LIRG Survey (GOALS – Díaz-Santos et al. 2013), a sample of LIRGs at $z < 0.09$.

In what follows, we adopt a Kroupa initial mass function (IMF – Kroupa & Weidner 2003) and a Λ cold dark matter cosmology with $H_0 = 70$ km s^{-1} Mpc^{-1}, $\Omega_M = 0.27$ and $\Omega_\Lambda = 0.73$.

2 SAMPLE SELECTION FOR PACS SPECTROSCOPY

We make use of the internal phase-1 data release (v2; Rigby et al. 2011; Smith et al. 2011, Valiante et al., in preparation, and Bourne et al., in preparation) taken from the three equatorial fields of the *Herschel*-Astrophysical Terahertz Large Area Survey (*H*-ATLAS[2]– Eales et al. 2010). We make use of both Spectral and Photometric Imaging Receiver (SPIRE; Griffin et al. 2010) and PACS *H*-ATLAS data (Pascale et al. 2011; Ibar et al. 2010). From the total number of 109 231 sources detected in these fields, we performed the following selection criteria for our targets: (1) a flux density threshold at $S_{160\,\mu m} > 150$ mJy, where 160 μm is near the peak of the spectral energy distribution (SED) of a local star-forming galaxy; (2) targets without PACS 160 μm ($>3\,\sigma$) neighbours within 2 arcmin from their centroids (to avoid problems when chopping; see Section 3); (3) an unambiguously identification in the Sloan Digital Sky Survey (SDSS DR6 – Adelman-McCarthy et al. 2008) (RELIABILITY >0.8, Smith et al. 2011, Bourne et al., in preparation.); (4) galaxies need to be smaller than the PACS spectroscopic field of view, so restricted to sources with Petrosian SDSS radii smaller than 15 arcsec in the *r* band; (5) high-quality spectroscopic redshifts from the Galaxy and Mass Assembly survey (GAMA[3] – Driver et al. 2009, 2011) (Z_QUAL ≥ 3). Note that GAMA combines spectra from SDSS with deeper spectra taken with the AAOmega fibre-fed spectrograph on the 3.9-m Anglo-Australian Telescope; (6) a redshift between $0.02 < z < 0.2$ (median, 0.05), where the upper limit is imposed by the point at which the [C II] emission is redshifted to the edge of the PACS spectrometer 160 μm band (which is known to leak), and the lower limit is imposed by the Petrosian *r*-band criterion. Applying all these criteria, we remain with a sample of 327 sources.

For each field, we randomly selected galaxies to span a wide range of optical morphological types and IR luminosities. In total, we selected a statistically significant sample of 84 galaxies for a [C II] spectroscopic campaign using *Herschel*-PACS during its second open time call. Galaxies have photometric detections at 100, 160, 250, 350 and 500 μm by *Herschel*, including *Wide-field Infrared Survey Explorer* (*WISE* – Wright et al. 2010) photometry, and approximately half of them were also detected by *IRAS* at 60 μm (using the Revised Imperial *IRAS*–FSC Redshift Catalogue[4], RIFSCZ_SHORT.V2; Wang et al. 2014). The combination of *IRAS/WISE/Herschel*/SDSS photometry and GAMA spectroscopy allows accurate estimates for a wide range of physical parameters, including L_{IR} (having a range of $10^{10} < L_{IR}/L_\odot < 10^{12}$), dust temperature, stellar masses, emission line strengths, metallicities, etc. (see Section 4).

3 PACS IFU OBSERVATIONS AND DATA ANALYSIS

Data were obtained between 2013 April 18 and 28, a few weeks before *Herschel* ran out of liquid helium, for the *Herschel* Open Time project, OT2_EIBAR_1 (P.I. E. Ibar). Of the parent sample of 84 galaxies, 28 were observed (Table 1), all from only one of the equatorial *H*-ATLAS coverages – the GAMA-09 h field. The selection of these 28 was performed purely on the basis of scheduling efficiency, so this sample is representative of the parent sample, just smaller in number (see Fig. 1).

We targeted the redshifted [C II]-157.7 μm line emission using PACS spectroscopy in the first order/R1 filter. PACS comprises an array of 5 × 5 spaxels, 9.4 arcsec × 9.4 arcsec each, covering ∼2 μm of bandwidth covered. The instantaneous field of view in a single pointing (pointed-mode) observation is thus 47 arcsec × 47 arcsec, hence based on the optical size, the majority of the line emission falls on the central spaxel.

The observations were made with a small chopping angle (1.5 arcmin), as appropriate for our sources. Note that our selection criteria have ensured that no sources would lie in the chopped beam. The *H*-ATLAS survey targeted areas of low IR background, so that the background intensities never approached the detector saturation level.

We retrieved the calibrated PACS level-2 data products (processed with SPG v12.1.0) using the *Herschel* User Interface[5] (HUI v6.0.4). We exported the HPS3DRB (blue) and HPS3DRR (red) data cubes, including the appended signal, coverage, noise and wavelength index. These data cubes comprise 5 × 5 spaxels × n_{chan} rebinned spectral channels for each observed galaxy. At the observed frequencies, the effective spectral resolution is ∼190–240 km s^{-1}, providing useful kinematical information for typical disc-like galaxies (see Table 3). We use the Interactive Data Language (IDL) to analyse these cubes along with the wavelength index array.

First, we find the best flux density measurement by comparing the central spaxel line emission (plus an aperture correction ∼0.4–0.5; a point-like estimate) with the summed over the whole IFU (extended estimate). We conclude that the best compromise in terms of signal to noise for the line flux density is to use the weighted sum (aided by the appended instrumental noise cube) of the central 3 × 3 spaxels. The addition of the outer spaxels only introduced noise in the signal. We recover, on average, 10 per cent more flux in the extended estimate than in the point-like one.

[C II] line fluxes were measured via a Gaussian fit to the added spectra (see Fig. 2), fitting simultaneously a linear background slope and a Gaussian using the MPFITPEAK routine within IDL. To perform the fit, we removed channels suffering from higher noise in both ends of the spectrum.

Using the spectroscopic redshifts, we calculate [C II] luminosities following Solomon & Vanden Bout (2005). In order to estimate uncertainties for the line parameters, we ran a Monte Carlo realization (1000 ×), randomly varying the signal per spectral channel using the instrumental error cube. Based on these simulated data, we quote 1σ uncertainties for the line measurements and 3σ upper limits (based on intrinsic 400 km s^{-1} FWHM widths) in Table 3.

We opted to receive data in order/B3 (blue filter at 70 μm) rather than order/G2 (green), as we already have 100-μm continuum photometry from the *H*-ATLAS imaging survey. This PACS blue point was expected to be used to improve the photometric SED sampling

Table 1. Log of PACS spectroscopic observations. Each observation lasted 394 s and was processed with SPG version 12.1.0. The table shows the IAU name, *H*-ATLAS's nickname, GAMA identifier and the OBSID during the *Herschel* campaign.

IAU name	Nickname	GAMA ID	OBSID
HATLAS J09:17:21.91+00:19:18.8	G09.v2.117	601323	1342271048
HATLAS J09:12:05.82+00:26:55.5	G09.v2.42	216401	1342270763
HATLAS J09:09:49.59+01:48:45.9	G09.v2.26	324842	1342270761
HATLAS J09:07:50.13+01:01:42.6	G09.v2.107	279387	1342270762
HATLAS J09:05:32.66+02:02:20.0	G09.v2.58	382362	1342270757
HATLAS J09:00:04.98+00:04:46.7	G09.v2.55	209807	1342270755
HATLAS J08:58:35.96+01:31:48.9	G09.v2.76	376679	1342270657
HATLAS J08:58:28.62+00:38:14.8	G09.v2.80	622694	1342270756
HATLAS J08:57:48.00+00:46:41.2	G09.v2.48	622662	1342270656
HATLAS J08:54:50.33+02:12:08.9	G09.v2.38	386720	1342270658
HATLAS J08:54:06.05+01:11:30.5	G09.v2.137	301346	1342270655
HATLAS J08:53:56.59+00:12:55.6	G09.v2.170	600026	1342270649
HATLAS J08:53:46.47+00:12:51.6	G09.v2.45	600024	1342270648
HATLAS J08:53:40.87+01:33:48.1	G09.v2.103	323855	1342270654
HATLAS J08:52:34.39+01:34:19.8	G09.v2.87	323772	1342270653
HATLAS J08:51:12.83+01:03:43.6	G09.v2.235	371789	1342270651
HATLAS J08:51:11.48+01:30:06.9	G09.v2.60	376293	1342270652
HATLAS J08:49:07.15−00:51:40.2	G09.v2.175	3624571	1342270647
HATLAS J08:46:30.79+00:50:55.1	G09.v2.90	278475	1342270650
HATLAS J08:44:28.41+02:03:49.8	G09.v2.52	345754	1342270371
HATLAS J08:44:28.27+02:06:57.3	G09.v2.77	386263	1342270370
HATLAS J08:43:50.90+00:55:34.0	G09.v2.102	371334	1342270372
HATLAS J08:43:05.18+01:08:57.0	G09.v2.167	300757	1342270373
HATLAS J08:42:17.71+02:12:22.3	G09.v2.232	867786	1342270365
HATLAS J08:41:39.45+01:53:44.8	G09.v2.299	345647	1342270364
HATLAS J08:38:32.01+00:00:44.5	G09.v2.111	208589	1342270374
HATLAS J08:37:45.33−00:51:42.3	G09.v2.66	3895257	1342270362
HATLAS J08:36:01.57+00:26:18.1	G09.v2.23	214184	1342270363

of the targets. We explored the blue spectra in the 53–63 μm range (depending on the source redshift) and found no clear signs of line emission in the data cubes, as expected. The significance of the continuum level (blue and red) was not high enough to permit a reliable photometric point for our SED fitting approach.

4 RESULTS

4.1 SED properties

Making use of the *Herschel*-PACS, *Herschel*-SPIRE, and the publicly available broad-band measurements from *WISE*-22 μm (all targets detected) and *IRAS* (17 sources reliably detected at 60 μm), we fitted the SED of each galaxy following a similar approach as in Ibar et al. (2013). We fit a usual modified blackbody (MBB) but forcing the SED shape to a power law in the high-frequency range of the spectra. The fits are aided by the known optical redshifts. We shift all SEDs to rest-frame frequencies, following ($\nu = \nu_{obs}\,[1 + z]$), and then fit the following parametrization

$$S_\nu(\nu) = A \times \begin{cases} \mathrm{MBB}(\nu) & \text{if } \nu \leq \nu_\star \\ \mathrm{MBB}(\nu_\star) \times (\nu/\nu_\star)^{-\alpha_{\mathrm{mid-IR}}} & \text{if } \nu > \nu_\star \end{cases} \quad (1)$$

where

$$\mathrm{MBB}(\nu) = \frac{\nu^{3+\beta}}{\exp\left(\frac{h\,\nu}{k\,T_{\mathrm{d}}}\right) - 1}. \quad (2)$$

The *h* and *k* parameters refer to Planck and Boltzmann constants, respectively. β is the usually called dust emissivity index (e.g. Seki & Yamamoto 1980; Dunne et al. 2011) – an averaged property of

the dust grain emission over of whole galaxy. The parameter $\nu_\star$ is obtained numerically at

$$\frac{\mathrm{d}\log_{10}(\mathrm{MBB})}{\mathrm{d}\log_{10}(\nu)}(\nu_\star) = \alpha_{\mathrm{mid-IR}} \quad (3)$$

which is simply used to match the slope of the MBB function with the high-frequency power-law (roughly at ∼100–200 μm). This parameter does not have a physical meaning, nevertheless it is useful to account for the mid-IR part of the spectra which otherwise is underestimated by a simple MBB (see Appendix A). Examples of best-fitting SED are shown in Fig. 2. To measure the IR luminosity, $L(8-1000\,\mu\mathrm{m})$, we integrate the best fitted SED in rest-frame frequencies between $\nu_1 = 0.3$ THz (1000 μm) and $\nu_2 = 37.5$ THz (8 μm),

$$L(8-1000\,\mu\mathrm{m}) = 4\pi\,D_{\mathrm{L}}^2(z) \int_{\nu_1}^{\nu_2} S_\nu\,\mathrm{d}\nu \quad (4)$$

Under this parametrization, we obtain the dust temperature (T_{d}), the dust emissivity index (β), the mid-IR slope ($\alpha_{\mathrm{mid-IR}}$), and the normalization which provides the total IR luminosity (rest frame 8–1000 μm). Uncertainties for each parameter were obtained from a Monte Carlo simulation (100 times), randomly varying the broadband photometry as appropriate for their measured uncertainties (Table 3). The best-fitting SEDs for all our target galaxies are shown in Fig. 2. We find that our sample have luminosities of the order of $10 < \log_{10}(L_{\mathrm{IR}}/L_{\odot}) < 12$, dust temperatures of $20 < T_{\mathrm{d}}/\mathrm{K} < 55$, mid-IR slopes in the range of $1.5 < \alpha_{\mathrm{mid-IR}} < 3.2$ (plus two outliers at ∼4.5), and dust emissivity indices of $0.3 < \beta < 2.5$.
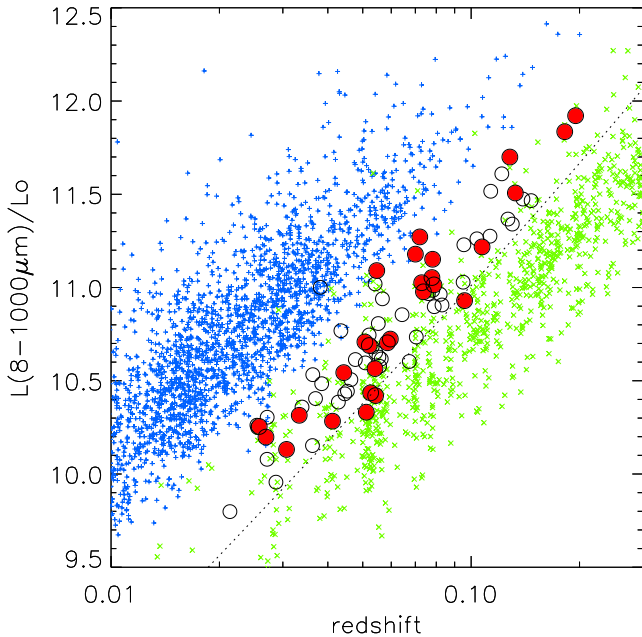
Figure 1. IR luminosity versus redshift for the 28 galaxies that were observed with PACS for [C II] spectroscopy (large red circles) and the full parent sample of 84 sources (black empty circles). Our targets cover approximately two orders of magnitude in L_{IR}. We overplot the Revised Imperial *IRAS*–FSC Redshift Catalogue of Wang et al. (2014) [blue crosses; considering $L(8\text{-}1000\,\mu m)/L_{\odot} = 4\pi D_L^2 \times S_{IR}$, where $S_{IR} = 1.8 \times 10^{-14}$ (13.48 $S_{12\,\mu m}$ + 5.16 $S_{25\,\mu m}$ + 2.58 $S_{60\,\mu m}$ + $S_{100\,\mu m}$) W m^{-2}; Sanders & Mirabel 1996, and the observed *H*-ATLAS sources in the GAMA-09h field (green crosses). The dotted line shows the detection threshold used to select our targets, above which sources were randomly selected (any objects lying below the threshold are due to an improved SED fitting approach that was implemented post-selection, resulting in slightly lower L_{IR} estimates). The detection threshold was applied to ensure a > 5σ line detection within 10 min using the simplest (single scan, single pointing) PACS spectroscopic mode, i.e. $S_{[C\,II]} > 15.5 \times 10^{-18}$ W m^{-2} assuming [C II]/IR = 0.001.

4.2 The [C II] deficit

Like many before us, we find that [C II] luminosity (including PDR and non-PDR components, which cannot be disentangled in this study) correlates strongly with L_{IR} luminosity over approximately two orders of magnitude (Fig. 4). A simple linear regression (excluding [C II] undetections) results in $\log_{10}(L_{[C\,II]}/L_{\odot}) = (0.721 \pm 0.003) \times \log_{10}(L_{IR}/L_{\odot}) + (0.53 \pm 0.04)$ and the distribution has a Spearman's rho rank correlation coefficient of 0.88 and a two-sided significance of its deviation from cero of 2×10^{-7}. The slope of this correlation evidences the so-called [C II] deficit, i.e. at higher IR luminosities the line to continuum ratio decreases.

4.3 Correlations with dust properties

The quality of our data permits us to explore dust temperatures in great detail (uncertainties range from 1 to ∼5 K based on Monte Carlo simulations; see Table 3). This is a major step forward compared to previous studies that only provided a proxy for the dust temperature, e.g. using the *IRAS* 100 μm to 60 μm ratio (Malhotra et al. 2001). Within our sample, most of the low-luminosity, low-redshift galaxies with $L_{IR} \lesssim 10^{11}$ L$_{\odot}$, have isothermal dust temperatures of $T_d = 23 \pm 1$ K (Fig. 5) – typical of 'normal' *H*-ATLAS galaxies (e.g. Smith et al. 2013). The galaxies

with cooler dust ($T_d < 30$ K) tend to have ∼ 2 × higher [C II]/IR ratios than warmer galaxies. We find that ∼90 per cent of the galaxies with $T_d < 30$ K have [C II]/IR >3 × 10^{-3}. This fraction decreases to ∼20 per cent for hotter galaxies.

It is interesting to note the mild correlation where flatter mid-IR slopes tend to produce lower [C II]/IR ratios. This might be a manifestation for the presence of stronger radiation fields contributing to the 22 μm flux density, or simply due to the poor mid-IR constraints on the SED-fitting approach (see also Section 4.4). We find that the fitted dust emissivity index, β, correlates with the [C II]/IR ratio, where higher β values are found in galaxies with higher [C II]/IR ratios (Fig. 5). In Table 2, we explore various possible correlations for the [C II]/IR ratio as a function of fitted and observed quantities.

4.4 Correlations with *WISE* colours

Fig. 6 shows a colour–colour diagram using *WISE* and *Herschel* photometry for our sample. We find that low [C II]/IR ratios (< 2.5 × 10^{-3}) are almost ubiquitous among galaxies presenting a flux density ratio $S_{12\,\mu m}/S_{22\,\mu m} < 0.5$, i.e. a power law with $\alpha_{22}^{12} < -1.14$. Note that all of our galaxies got fitted α_{mid-IR} values which are steeper than -1.14 (see Fig. 5), implying that the *WISE* colours do not reflect the same mid-IR slope. In fact, Fig. 6 indicates that the [C II]/IR luminosity ratio depends strongly as a function of the 22 μm flux density (see also Table 2).

In Fig. 6, we also show the expected *WISE* and *Herschel* colours from different SED templates taken from Polletta et al. (2007) and convolved with *WISE* transmission filters in the redshift range of this study ($z < 0.2$). We find that mid-IR templates from star-bursting galaxies (e.g. NGC 6240) and moderately luminous AGNs (e.g. Sey2) are well suited to explain low $S_{12\,\mu m}/S_{22\,\mu m}$ ratios (i.e. lower [C II]/IR ratios). Higher [C II]/IR ratios tend to be better explained by spiral *Hubble*-type galaxies (S0–Sc). A close inspection to their mid-IR to far-IR SEDs, suggests three signatures controlling the $S_{12\,\mu m}/S_{22\,\mu m}$ ratio; the strength of the PAH 7.7 μm emission line system, the Silicate absorption band at 9.8 μm and the slope of the spectra. Unfortunately, with the present data we are unable to distinguish between these different features. We have performed a basic simulation taking into account the broad-band filters and artificial SEDs including different slopes, equivalent widths of the PAH emission and Si absorption band. We find that the mid-IR slope is probably the dominant component in varying the observed $S_{12\,\mu m}/S_{22\,\mu m}$ ratio. On the other hand, on average, galaxies with low (high) [C II]/IR ratios have low (high) $S_{3.4\,\mu m}/S_{4.6\,\mu m} \approx 1.3$ (1.45) ratios. Based on Polletta et al.'s templates, we find that *WISE* colours from elliptical, or normal early-type galaxies, or powerful AGNs, lie outside Fig. 6, in agreement with the far-IR selection criteria which prefers star-forming dusty galaxies.

4.5 Correlations with optical properties

In this section, we explore the optical properties of the targets. First, we look for morphological features. We downloaded the corresponding FITS files *r*-band images from the SDSS archive[6] (see Fig. 3). We masked all sources which are not contributing to the far-IR emission, and created the encircled energy fraction as a function of a radius centred at the peak source position. We measured the effective radius at which 50 per cent (and 90 per cent) of the power is encircled, and then transformed this projected size into a physical

---

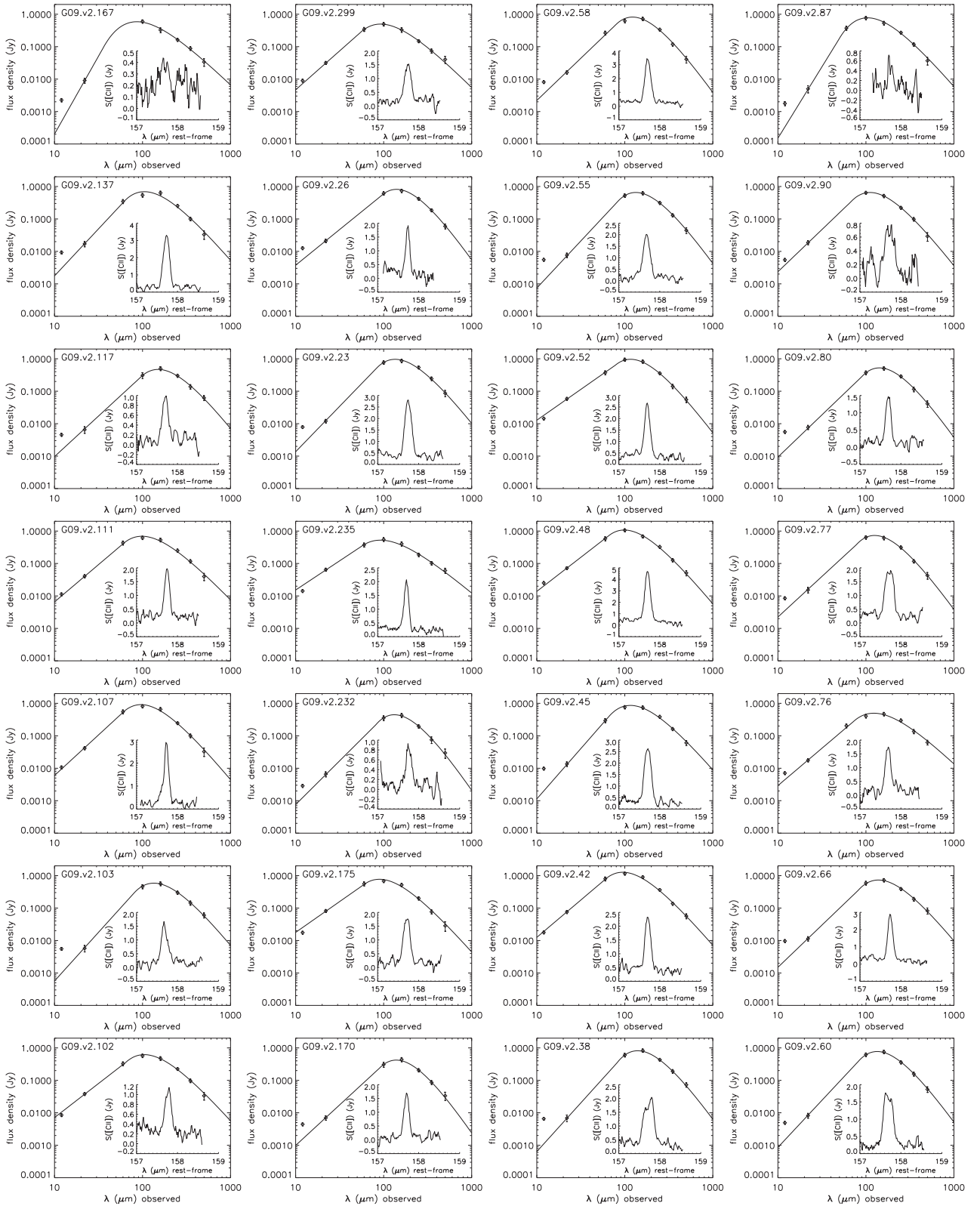[6] SKYSERVER.SDSS3.ORG/DR9/EN/TOOLS/CHART/

Figure 2. The flux densities versus observed wavelengths for all 28 galaxies presented in this work. From short to long wavelengths, SED data points correspond to broad-band photometry from: *WISE* 12 and 22 μm, *IRAS* 60 μm, *Herschel* PACS 100, 160, and *Herschel* SPIRE 250, 350, and 500 μm. Note that *WISE* 12 is not used to fit the SED. All photometric points have significance above 3σ limit. The inset in each panel shows the [C II] spectra, flux density versus rest-frame wavelength, observed by the central spaxel of the PACS detector. Only two galaxies (G09.v2.87 and G09.v2.167) resulted with a [C II] peak to noise line ratio lower than three. These two galaxies appear as upper limits in the following figures.

Table 2. The correlation of the $L_{[C\,II]}/L_{IR}$ luminosity ratio as a function of various different parameters. Linear regression values, where $L_{[C\,II]}/L_{IR} = a + b \times \psi$, are obtained by simple χ^2 minimization. We exclude the two [C II] undetections from this analysis. Last two columns show the Spearman's rho (ρ) rank correlation and the two-sided significance of its deviation from cero (Q). We provide values for the best linear fit, only when a significant correlation is found $Q < 5$ per cent.

ψ	a	b	ρ	Q(per cent)
$\log_{10}[L_{IR}(L_\odot)]$	-0.7121 ± 0.1021	-0.1713 ± 0.0094	-0.49	1.1
T_{dust} (K)	-1.9803 ± 0.0180	-0.0182 ± 0.0005	-0.72	0.0
α_{mid-IR}	-3.5550 ± 0.0256	0.4082 ± 0.0105	0.75	0.0
β	-2.8705 ± 0.0141	0.2084 ± 0.0094	0.52	0.7
$\log_{10}[L_{22\,\mu m}(\text{erg s}^{-1}\,\text{Hz}^{-1})]$	4.9372 ± 0.2326	-0.2388 ± 0.0074	-0.76	0.0
$\log_{10}[L_{100\,\mu m}(\text{erg s}^{-1}\,\text{Hz}^{-1})]$	1.4705 ± 0.3232	-0.1231 ± 0.0098	-0.42	3.3
$\log_{10}[L_{160\,\mu m}(\text{erg s}^{-1}\,\text{Hz}^{-1})]$	–	–	-0.31	12.8
$\log_{10}[L_{250\,\mu m}(\text{erg s}^{-1}\,\text{Hz}^{-1})]$	–	–	-0.26	19.2
$\log_{10}[L_{350\,\mu m}(\text{erg s}^{-1}\,\text{Hz}^{-1})]$	–	–	-0.26	19.3
$\log_{10}[L_{500\,\mu m}(\text{erg s}^{-1}\,\text{Hz}^{-1})]$	–	–	-0.25	21.4
$L_{3.4\,\mu m}/L_{4.6\,\mu m}$	-3.4390 ± 0.0329	0.6224 ± 0.0234	0.62	0.1
$L_{12\,\mu m}/L_{22\,\mu m}$	-2.9487 ± 0.0096	0.8443 ± 0.0194	0.87	0.0
$L_{22\,\mu m}/L_{100\,\mu m}$	-2.2960 ± 0.0079	-5.5447 ± 0.1360	-0.82	0.0
$r_{eff,\,50\,per\,cent}$(kpc)	–	–	0.19	36.4
$r_{eff,\,90\,per\,cent}$(kpc)	–	–	-0.04	82.8
$\log_{10}[\Sigma_{IR}(L_\odot/\text{kpc}^2)]$	-0.3570 ± 0.0792	-0.2462 ± 0.0088	-0.65	0.0

scale at the given redshift of the galaxy. These scales are shown in Fig. 7 as a function of the [C II]/IR ratio. No clear correlation is found between these two observables (Table 2).

We then performed a basic visual inspection using the *r*-band SDSS imaging to classify these galaxies in three populations: ellipticals ('E'), spirals ('S') and irregulars ('I'). Some galaxies show morphologies which are not possible to classify in a single population. In these cases, we use a combination of letters, e.g. 'ES' or 'EI', to refer to a prominent bulge with a disc or an irregular morphology, respectively. Under this classification, in Fig. 7 we show that the [C II]/IR ratio is preferentially higher in galaxies presenting a prominent disc compared to those which do not present discy morphologies.

In order to provide an estimate for the IR surface brightness of the galaxies, we consider the optical *r*-band radius as a proxy for the actual IR radius, so we define $\Sigma_{IR} = L_{IR}/(2\pi r_{eff,\,50\,per\,cent}^2)$. We reckon this is a strong assumption so this value should be interpreted with caution. As expected, we find that the previous morphological classification is correlated to the surface brightness. Indeed, those with low Σ_{IR} values tend to be those presenting disc-like morphologies, while those which are classified as pure elliptical tend to be those with highest brightness in the sample.

With the aim to identify possible [C II] self-absorption (e.g. following Gerin et al. 2015), we have looked for the properties of edge-on galaxies within the spiral population (see Fig. 3). The four identified edge-on galaxies tend to have a well-defined high [C II]/IR ratios of 3.5×10^{-3}, and do not deviate from the rest of the 'spiral-only' population.

To characterize the nature of our galaxies, we have utilized the SDSS and GAMA spectra to locate them in the 'Baldwin, Phillips & Terlevich' (BPT) diagram (Baldwin, Phillips & Terlevich 1981). Emission line strengths for Hα, Hβ, [N II]λ6583 and [O III]λ5007 are extracted from spectra using the GANDALF pipeline (see details in Hopkins et al. 2013). Only two galaxies do not have all four lines detected. We show these data in Fig. 8, where our sample is overplotted on top of the whole spectroscopic SDSS population. We find that our sample locates all over the star forming, AGN and composite (a mix of both) regions. The main selection criterion, $S_{160\,\mu m} > 150$ mJy,

therefore introduces a significant number of low-luminosity AGNs in the sample. This permits to test if AGN activity plays an important role in the [C II]/IR ratio. Note that none of our galaxies falls close to the peak of the distribution of star-forming SDSS galaxies. We show that under the BPT classification, our sample of star forming and composite galaxies do not show significant differences in terms of [C II]/IR ratios (Fig. 8). We note, however, that the uncertainties in the line flux ratios might be blurring any possible correlation.

The stellar masses ($M_\star$) for all galaxies are calculated as described in Taylor et al. (2011), using GAMA catalogue version v08. The stellar mass estimates were derived by fitting their SEDs (Bruzual & Charlot 2003) to the SDSS *ugriz* imaging – data which have been re-processed by the GAMA team (Hill et al. 2011). The dust obscuration law applied was that of Calzetti et al. (2000), and a Chabrier (2003) IMF was assumed. The stellar masses are determined by integrals that are weighted to the probability of each SED fit. This has been performed to all galaxies regardless of the nature (star forming/AGN) defined by the BPT diagram. We have not applied any conversion factor to convert from Chabrier to Kroupa IMF because the variation is negligible compared to the measured errors. Taylor et al. demonstrate that the relation between (*g*–*i*) and $M_\star/L$ offers a simple indicator of the stellar masses. To account for aperture effects, a correction based on the Sérsic fit to the surface brightness profiles is applied to the stellar masses (see Taylor et al. 2011; Kelvin et al. 2012).

We use the SFR derived from the bolometric IR emission, following Kennicutt (1998). In combination with the stellar mass estimate, we obtain the specific-SFRs (sSFR = $\text{SFR}_{IR}/M_\star$). We find the sSFR seems to anticorrelate with the [C II]/IR luminosity ratios (see Fig. 9), hence those galaxies presenting lower [C II]/IR ratios are preferentially passing through more violent bursts of star formation. In order to remove a possible dependence on redshift and following Díaz-Santos et al. (2013)'s work, we have divided our sSFR estimates by the one expected at the 'main-sequence' defined by Elbaz et al. (2011, at the given redshift). We find that our sources are centred at the main sequence value but cover a wide range of two orders of magnitude around it (see Fig. 9). If we compare our

Table 3. Properties of the targets analysed in this work. Column 1: *H-ATLAS's* nickname; Column 2: GAMA's redshift; Column 3: line peak flux; Column 4: intrinsic line FWHM width obtained after removing (in quadrature) the instrumental spectral resolution; Column 5: line flux density ($\sqrt{2\pi} \times P_{[CII]} \times \sigma_{[CII]}$, where $\sigma_{[CII]} = FWHM_{[CII]}/2.355$); Column 6: line luminosity; Column 7: IR (8–1000 μm) luminosity; Column 8: dust temperature; Column 9: dust emissivity index; Column 10: mid-IR slope; Column 11: $L_{[CII]}/L_{IR}$ luminosity ratio, where upper limits are 3σ assuming an intrinsic 400 km s⁻¹ FWHM width; Column 12: effective radius at which 50 per cent of the power is encircled using SDSS *r*-band imaging; Column 13: stellar mass; Column 14: specific SFR using the IR luminosity as proxy; Column 15: metallicity measurements for star-forming galaxies; Column 16: BPT classification, 0=star forming, 1=composite and 2=AGN; Column 17: optically based visual morphological classification, E=elliptical, S=spiral and I=irregular.

| Target	z	$P_{[CII]}$ (Jy)	$FWHM_{[CII]}$ (km s⁻¹)	$S_{[CII]}$ (Jy km s⁻¹)	$L_{[CII]}$ ($\times 10^8 L_\odot$)	$\log_{10}(L_{IR}/L_\odot)$	T_{dust} (K)	β	α_{mid-IR}	[C II]/IR ($\times 10^{-3}$)	$r_{eff,50 per cent}$ (kpc)	$\log_{10}(M_\star/M_\odot)$	$sSFR_{IR}$ (Gyr⁻¹)	$12+\log_{10}(O/H)$	BPT class	Morph.
(1)	(2)	(3)	(4)	(5)	(6)	(7)	(8)	(9)	(10)	(11)	(12)	(13)	(14)	(15)	(16)	(17)
G09.v2.102	0.073	1.90 ± 0.06	356 ± 22.88	849 ± 46	1.70 ± 0.09	11.03 ± 0.01	36 ± 2	1.2 ± 0.2	2.10 ± 0.06	1.60	3.5	10.63 ± 0.12	0.30	–	1	ES
G09.v2.103	0.041	4.45 ± 0.06	220 ± 0.10	1509 ± 31	0.95 ± 0.02	10.28 ± 0.03	25 ± 2	1.5 ± 0.4	3.00 ± 0.18	4.96	5.0	10.48 ± 0.12	0.08	–	1	S
G09.v2.107	0.128	4.50 ± 0.09	227 ± 21.31	1467 ± 62	9.33 ± 0.40	11.70 ± 0.01	39 ± 1	1.4 ± 0.1	2.50 ± 0.05	1.86	4.2	10.51 ± 0.13	1.84	8.923 ± 0.011	0	I
G09.v2.111	0.078	3.39 ± 0.07	192 ± 18.32	1052 ± 42	2.43 ± 0.10	11.15 ± 0.01	41 ± 2	0.9 ± 0.2	2.30 ± 0.06	1.72	5.1	10.55 ± 0.13	0.48	9.147 ± 0.013	0	ES
G09.v2.117	0.054	2.99 ± 0.06	168 ± 12.24	898 ± 31	0.99 ± 0.04	10.42 ± 0.04	22 ± 2	1.6 ± 0.3	2.50 ± 0.18	3.75	7.6	10.70 ± 0.12	0.06	–	–	ES
G09.v2.137	0.044	6.05 ± 0.06	284 ± 8.39	2349 ± 42	1.71 ± 0.03	10.54 ± 0.02	34 ± 2	1.3 ± 0.2	2.90 ± 0.17	4.90	2.5	10.13 ± 0.13	0.31	9.010 ± 0.006	0	ES
G09.v2.167	0.078	0.46 ± 0.05	–	–	< 1.25	11.05 ± 0.03	50 ± 2	0.7 ± 0.1	4.80 ± 0.20	<1.10	2.5	10.35 ± 0.14	0.61	–	2	E
G09.v2.170	0.051	4.52 ± 0.07	195 ± 12.97	1439 ± 38	1.41 ± 0.04	10.33 ± 0.03	21 ± 2	2.2 ± 0.5	2.50 ± 0.13	6.54	4.4	10.26 ± 0.13	0.14	–	–	S
G09.v2.175	0.070	3.03 ± 0.06	312 ± 17.73	1235 ± 46	2.28 ± 0.09	11.18 ± 0.01	42 ± 2	1.2 ± 0.2	1.90 ± 0.05	1.51	3.4	10.48 ± 0.11	0.60	–	1	E
G09.v2.232	0.096	2.15 ± 0.07	184 ± 0.01	648 ± 32	2.28 ± 0.11	10.93 ± 0.04	23 ± 3	2.2 ± 0.6	2.70 ± 0.20	2.67	7.5	–	–	–	1	ES
G09.v2.235	0.027	3.11 ± 0.07	142 ± 19.93	901 ± 34	0.24 ± 0.01	10.20 ± 0.01	50 ± 4	0.3 ± 0.2	1.80 ± 0.05	1.53	1.6	9.94 ± 0.11	0.22	8.665 ± 0.000	0	ES
G09.v2.23	0.033	5.25 ± 0.05	356 ± 8.34	2373 ± 44	0.97 ± 0.02	10.31 ± 0.02	24 ± 2	1.6 ± 0.4	2.80 ± 0.13	4.72	3.6	10.55 ± 0.11	0.07	8.935 ± 0.007	0	ES
G09.v2.26	0.182	4.56 ± 0.13	103 ± 23.42	1052 ± 51	13.81 ± 0.68	11.84 ± 0.02	24 ± 1	2.1 ± 0.2	2.20 ± 0.08	2.02	6.4	11.25 ± 0.12	0.46	9.142 ± 0.007	0	EI
G09.v2.299	0.074	2.44 ± 0.06	258 ± 25.34	880 ± 48	1.81 ± 0.10	10.98 ± 0.01	45 ± 3	0.8 ± 0.2	2.40 ± 0.08	1.91	2.3	10.54 ± 0.11	0.33	9.214 ± 0.012	0	E
G09.v2.38	0.059	2.94 ± 0.05	527 ± 16.39	1794 ± 58	2.30 ± 0.08	10.70 ± 0.02	22 ± 1	2.0 ± 0.3	3.00 ± 0.17	4.55	4.6	10.89 ± 0.11	0.08	9.115 ± 0.648	0	ES
G09.v2.42	0.055	3.89 ± 0.07	215 ± 17.74	1291 ± 43	1.45 ± 0.05	11.09 ± 0.01	38 ± 1	1.3 ± 0.1	2.30 ± 0.04	1.17	2.8	10.46 ± 0.12	0.51	–	1	E
G09.v2.45	0.051	6.10 ± 0.06	266 ± 7.28	2274 ± 41	2.18 ± 0.04	10.71 ± 0.01	31 ± 1	1.3 ± 0.2	3.10 ± 0.13	4.27	4.0	10.28 ± 0.13	0.32	8.901 ± 0.009	0	S
G09.v2.48	0.072	7.17 ± 0.07	223 ± 7.67	2398 ± 43	4.69 ± 0.09	11.27 ± 0.01	36 ± 1	1.4 ± 0.1	2.10 ± 0.03	2.51	2.4	10.58 ± 0.13	0.59	–	1	EI
G09.v2.52	0.026	4.35 ± 0.06	168 ± 11.33	1331 ± 33	0.33 ± 0.01	10.25 ± 0.01	27 ± 1	1.8 ± 0.3	1.90 ± 0.05	1.81	2.7	10.29 ± 0.11	0.11	–	2	ES
G09.v2.55	0.054	4.28 ± 0.07	296 ± 15.46	1697 ± 53	1.86 ± 0.06	10.57 ± 0.02	23 ± 1	2.0 ± 0.3	2.90 ± 0.11	5.05	3.3	10.81 ± 0.11	0.07	–	1	ES
G09.v2.58	0.052	5.41 ± 0.06	223 ± 9.54	1832 ± 39	1.86 ± 0.04	10.69 ± 0.02	25 ± 2	2.0 ± 0.4	2.60 ± 0.10	3.81	3.4	10.60 ± 0.12	0.15	9.086 ± 0.047	0	ES
G09.v2.60	0.060	3.52 ± 0.05	482 ± 13.53	1997 ± 55	2.66 ± 0.07	10.72 ± 0.02	23 ± 2	2.0 ± 0.4	2.90 ± 0.17	5.03	5.0	10.63 ± 0.12	0.15	–	1	S
G09.v2.66	0.031	6.73 ± 0.07	177 ± 8.13	2090 ± 35	0.73 ± 0.01	10.13 ± 0.03	24 ± 2	1.5 ± 0.3	2.60 ± 0.17	5.38	3.1	10.35 ± 0.12	0.07	–	1	S
G09.v2.76	0.107	3.61 ± 0.08	230 ± 18.52	1201 ± 47	5.30 ± 0.21	11.22 ± 0.01	36 ± 3	0.7 ± 0.2	2.30 ± 0.07	3.21	7.9	11.07 ± 0.12	0.17	–	2	EI
G09.v2.77	0.079	3.92 ± 0.06	403 ± 14.68	1917 ± 58	4.51 ± 0.14	11.01 ± 0.03	25 ± 2	2.0 ± 0.4	2.50 ± 0.18	4.38	4.6	10.59 ± 0.13	0.32	–	1	S
G09.v2.80	0.053	3.42 ± 0.07	104 ± 15.06	907 ± 32	0.94 ± 0.03	10.44 ± 0.02	21 ± 2	2.1 ± 0.4	2.60 ± 0.12	3.44	4.0	10.75 ± 0.12	0.06	–	1	E
G09.v2.90	0.133	1.70 ± 0.06	459 ± 55.95	909 ± 91	6.22 ± 0.63	11.51 ± 0.02	32 ± 3	1.6 ± 0.2	2.60 ± 0.16	1.93	4.7	10.73 ± 0.11	0.73	–	1	E
G09.v2.87	0.195	1.17 ± 0.12	–	–	<11.38	11.92 ± 0.01	39 ± 2	1.3 ± 0.2	4.40 ± 0.98	<1.36	3.3	10.59 ± 0.10	2.58	–	2	E
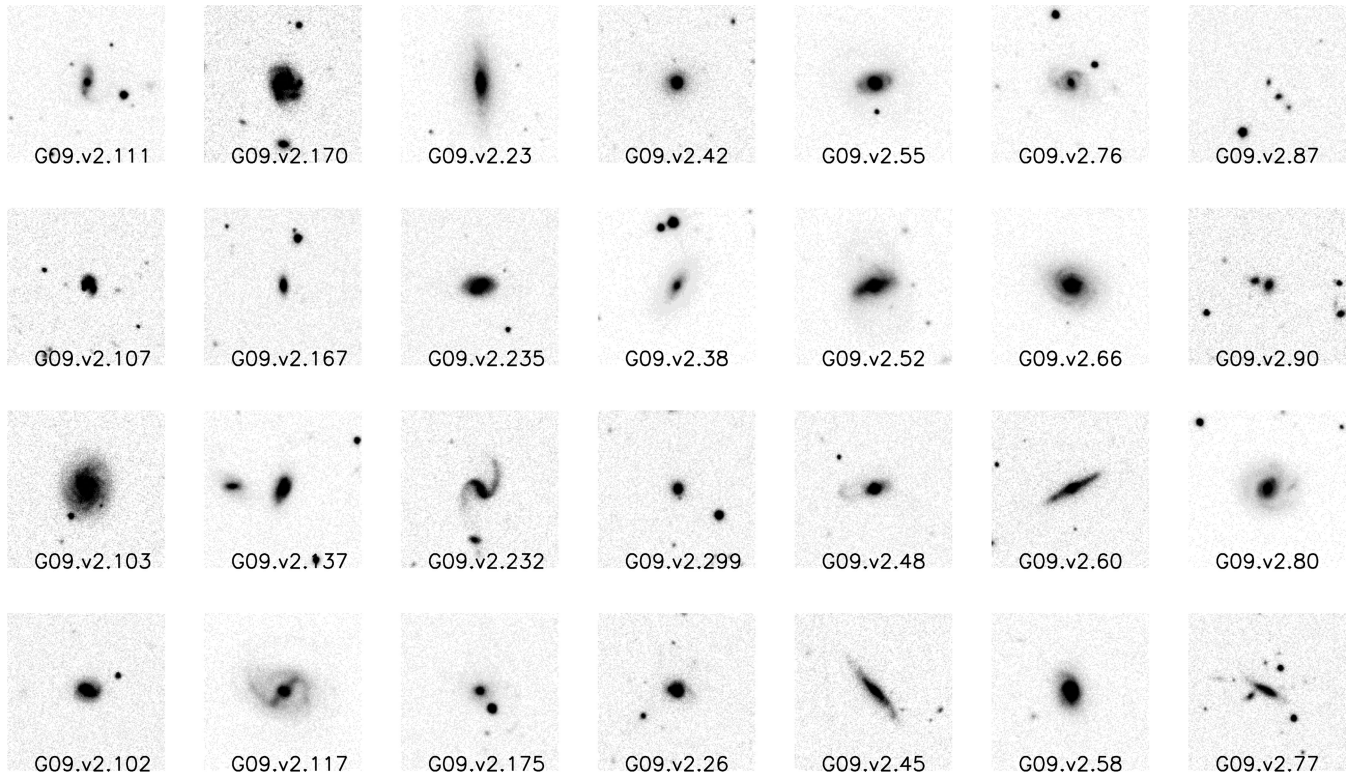
Figure 3. Postage-stamp images (1 arcmin × 1 arcmin) for our targets taken from the SDSS *r*-band imaging.
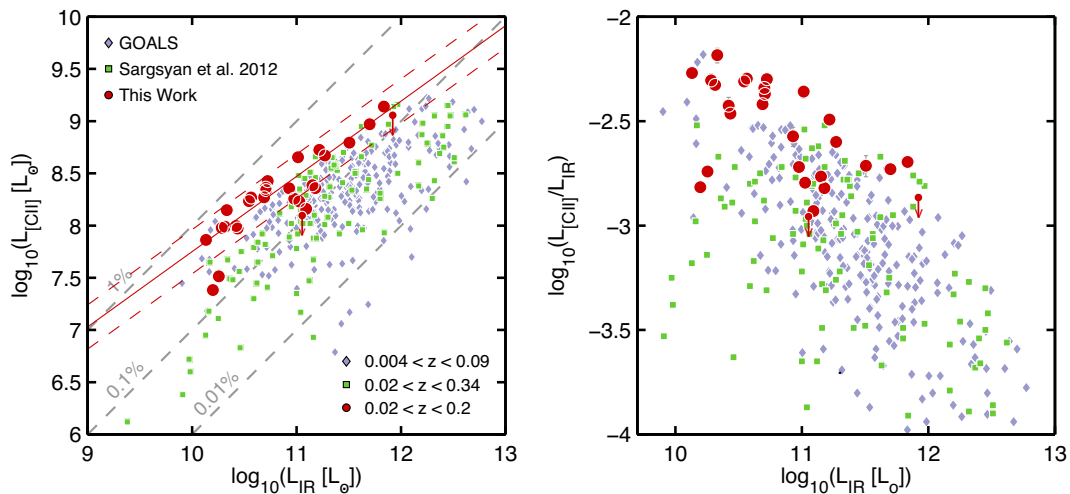

Figure 4. Left: [C II] line luminosity versus bolometric IR luminosity for the sample of sources presented in this work. We compare our observations to previous (at similar redshifts), GOALS (Díaz-Santos et al. 2013) and Sargsyan et al. (2012)'s samples. Díaz-Santos et al.'s data have been scaled by a 1.75 factor to convert from far-IR to IR luminosities (see Appendix E from Herrera-Camus et al. 2015). Continuum and dashed red lines show the best linear fit (excluding [C II] undetections) $\log_{10}(L_{[C II]}/L_{\odot}) = (0.721 \pm 0.003) \times \log_{10}(L_{IR}/L_{\odot}) + (0.53 \pm 0.04)$ and the 0.2 dex scatter, respectively. Diagonal lines show the 1.0, 0.1 and 0.01 per cent fraction of L_{IR}. Right: [C II]/L_{IR} as a function of L_{IR}, revealing the well-known [C II] deficit. Colour coded points are the same in both figures.

sample to Díaz-Santos et al.'s, our sample is more representative of 'normal' star-forming galaxies than theirs.

For those galaxies of which are defined as star forming in the BPT diagram (Fig. 8), we measure reliable metallicities using the O3N2 index of Pettini & Pagel (2004), and converting those values to the calibration of Tremonti et al. (2004), following Lara-López et al. (2013). We find that these star-forming galaxies present metallicities between $12 + \log_{10}(O/H) = 8.7$–9.2. For compar-

ison, Solar metallicity is 8.91. In low-metallicity environments $(12 + \log_{10}(O/H) < 8.1)$, the IR emission is expected to drop but the [C II] emission would remain almost invariant, therefore the [C II]/IR ratio is expected to be higher in low-metallicity environments (see also Rubin et al. 2009; De Looze et al. 2014). Nevertheless, our sample does not probe these lower metallicities (mainly due to dust selection criterion) and so we cannot investigate correlation of [C II] with metallicities.
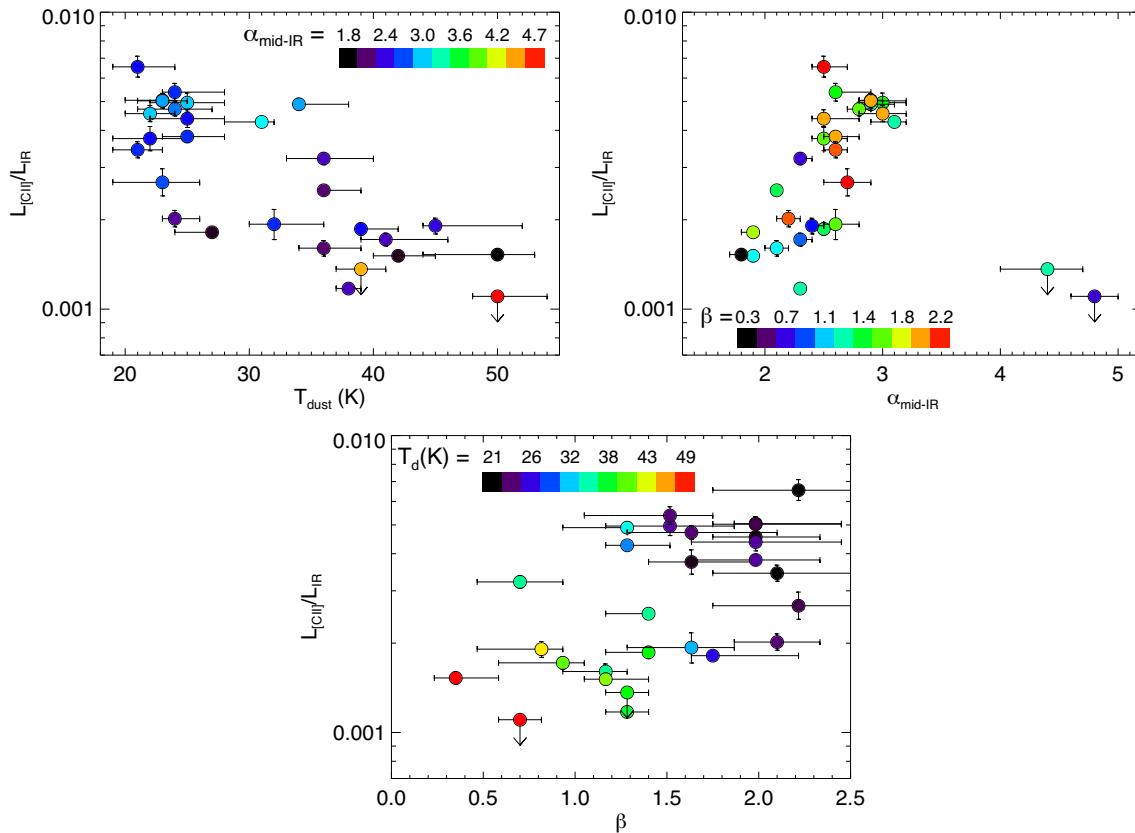
Figure 5. Dependence of the [C II]/IR luminosity ratio as a function of dust temperature (top-left; colour-coded in mid-IR index), mid-IR index (top-right; colour-coded in β) and dust emissivity β index (bottom; colour-coded in dust temperature). Data suggest that galaxies with colder dust temperatures tend to have higher [C II]/IR ratios than hotter galaxies.

5 DISCUSSION

For many years, it has been a great challenge to explain why there is a decrease in the [C II]/IR luminosity ratio towards bright ($L_{IR} > 10^{11} L_{\odot}$) IR luminosities. It is well established that this ratio has an intimate dependency on the strength of the radiation field ($\langle G_O \rangle$) and the density (n_e) of the ISM. As explained in Section 1, the [C II] emission comes from a whole range of different ISM states; ionized, atomic and/or molecular. Unfortunately, given the low resolution of our *Herschel* observations, these different components are impossible to disentangle directly from imaging. Fibre-based optical spectroscopy cannot spatially separate these components neither.

First of all, we look for possible biases introduced by the selection criteria used to construct our galaxy sample. We identify that one of the most important criterion is the flux density $S_{160\,\mu m} > 150$ mJy threshold, which introduces a strong selection effect on the redshift-luminosity distribution of the targets (see Fig. 1). Our targets span a redshift range between $z = 0.02$ and 0.2, so approximately 2.2 Gyr of cosmic time. Based on the measured sSFR, the galaxies in our sample double their stellar masses in scales of sSFR$^{-1} \approx 0.3$–20 Gyr (median 4 Gyr; see Fig. 9), values which are in most cases longer than 2.2 Gyr. In this work, we consider that for most of our targets the evolution is short in comparison to the redshift slide, i.e. a galaxy at fixed luminosity will be behaving the same at $z = 0.02$ as at $z = 0.2$. Only a fourth of the targets double their stellar masses in scales which are shorter than 2.2 Gyr (those ongoing more violent star-bursts). This assumption is necessary to alleviate the luminosity-redshift dependence seen in Fig. 1. In terms of the

ISM evolution using large samples of galaxies, Lara-López et al. (2009) finds no variation of the metallicity properties in this redshift range, nevertheless the dust mass density evolves strongly as a function of redshift, incrementing by a factor of 2 from $z = 0.02$ to 0.2 (Dunne et al. 2011). For the purposes of this work, we assume the flux density threshold at $S_{160\,\mu m} > 150$ mJy does not introduce biases on the results.

Significant differences are found between galaxies presenting high and low [C II]/IR luminosity ratios (see Table 2) – understood in this study as greater or lower than $\sim 2.5 \times 10^{-3}$. We find that galaxies with high ratios:

(i) have cold dust temperatures, preferentially lower than 30 K (see Fig. 5). This evidence indicates that these galaxies present a prominent IR component coming from extended ISM regions rather than compact ones located at the vicinity of powerful star-forming nuclear regions;

(ii) have a high *WISE* flux density ratio of $0.5 \lesssim S_{12\,\mu m}/S_{22\,\mu m} \lesssim 1.0$ (see Fig. 6). This range of mid-IR ratios tend to be associated with normal *Hubble*-type spiral galaxies, a ratio induced by a combination of spectral features within the broad *WISE* 12 µm and 22 µm filters: prominent PAH emission lines (not suppressed by strong radiation fields), a weak 10 µm Silicate absorption band (indicating moderate extinction levels), and an $\sim$22 µm spectra which does not seem to be dominated by powerful hot dust emission, e.g. a young and violent starburst or an AGN torus;

(iii) have preferentially lower surface brightness ($\Sigma_{IR} \lesssim 10^9$ L$_{\odot}$/kpc^2) as shown in Fig. 7 (see significance in Table 2). We stress this estimate uses the effective *r*-band radius
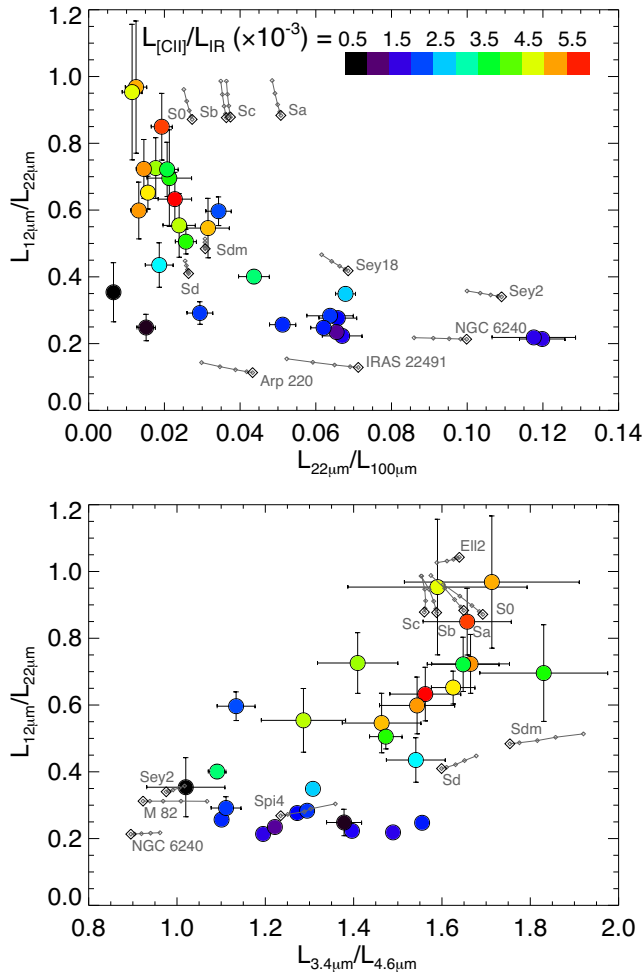
Figure 6. The figure shows the locus for our galaxies in a couple of colour–colour plots, exploiting *Herschel* and *WISE* photometry. Given the optical extension of the targets, we consider elliptical aperture photometry for the *WISE* photometry. Broad-band luminosities have not been k-corrected. Data points are colour-coded as a function of the [C II]/IR luminosity ratio (see top-bar in left-hand panel). We overplot also the expected colours for different SED templates taken from Polletta et al. (2007)'s libraries (convolved with response filters) in five redshift ranges ($z = 0$, 0.05, 0.1, 0.15 and 0.2) indicated by small diamonds, where the biggest one is at $z = 0$. The figure indicates that galaxies with highest [C II]/IR ratios are those with $0.5 < S_{12\,\mu m}/S_{22\,\mu m} < 1.0$, galaxies which could be explained by normal spiral 'Hubble'-class' galaxies (e.g. S0, Sa, Sb, Sc), while those with lower values are better represented by starburst templates such as Arp 220, M 82, IRAS 22491, NGC 6240, etc.

Figure 7. Top: [C II]/IR luminosity ratio as a function of effective radius in SDSS r-band (encircled fraction at 50 per cent in black and 90 per cent in red). Bottom: the variation of the [C II]/IR luminosity ratio as a function of surface brightness ($\Sigma_{IR} = L_{IR}/(2\pi r_{eff,50\,per\,cent}^2)$; here $r_{eff,\,50\,per\,cent}$ is based on the optical r-band size and Σ_{IR} has not been corrected by inclination), colour-coded as a function of a simply by-eye optical morphological classification; spirals ('S'), ellipticals ('E'), irregulars ('I'; including mergers), or composite morphologies. This figure clearly shows that higher [C II]/IR ratios are preferentially seen in galaxies presenting extended discs.

as a proxy for the IR extension. If the mean free path of the far-UV photons is large, then the strength of the radiation fields would be directly proportional to Σ_{IR} (Wolfire, Tielens & Hollenbach 1990). If this is the case, this suggests that galaxies with weaker radiation fields produce higher [C II]/IR luminosity ratios. Nevertheless, given the lack of correlation between [C II]/IR and r_{eff} (see Table 2), this behaviour could be a manifestation of the correlation with L_{IR} instead;

(iv) have preferentially disc-like morphologies. Those galaxies which are classified as spirals ('S'), without prominent bulges, are those with the highest [C II]/IR ratios ($\sim 4 \times 10^{-3}$; see Fig. 7), similar to that found by Díaz-Santos et al. (2013) while looking
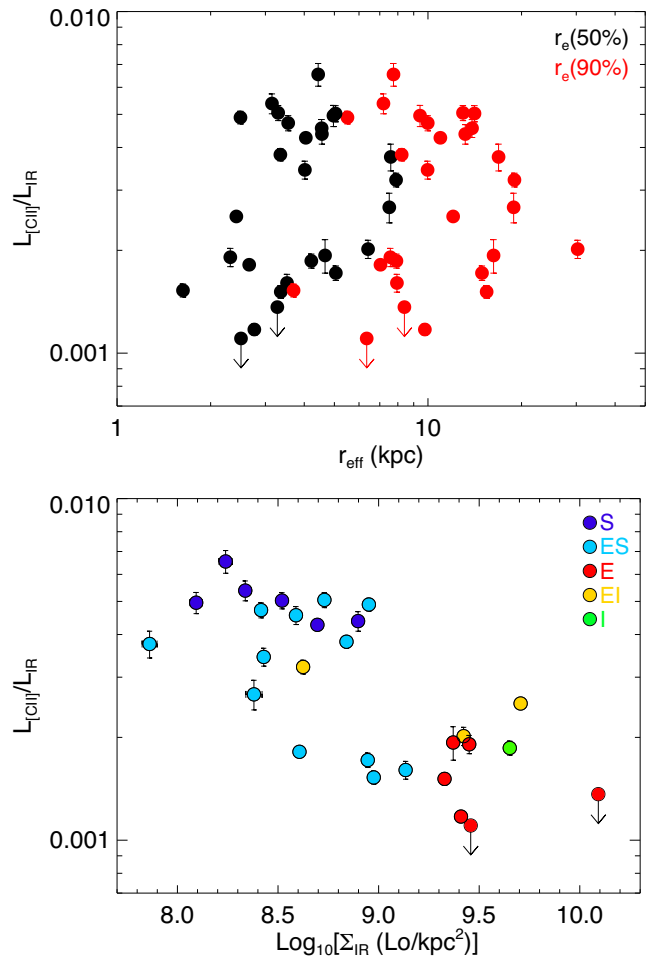
at the pure star-forming LIRGs in their sample. These evidences suggest that galaxies with high [C II]/IR ratios evolve quiescently rather than triggered by a major merger event with a subsequent powerful nuclear starburst;

(v) present a wide range of sSFR $\approx 5 \times 10^{-11}$–$3 \times 10^{-9}$ yr^{-1} (IR-based), hence the mechanism controlling the [C II] emission does not seem to relate to the efficiency of converting gas into stars. At constant SFR, these galaxies range from 3.3 to 20 Gyr to double their stellar masses. These results do not agree with the [C II]/IR versus sSFR/sSFR$_{MS}$ correlation (see Fig. 9) found by Díaz-Santos et al. (2013), probably because we observe more 'normal' galaxies (relative to the 'main-sequence' defined by Elbaz et al. 2011) than their local LIRGs sample, and also given by the fact that our sample does not include a significant number of galaxies with low [C II]/IR ratios that permit to evaluate the correlation at higher sSFR levels. Our data might suggest an evidence for a plateau in Díaz-Santos et al.'s correlation at sSFR/sSFR$_{MS}$ < 1, probably induced by a
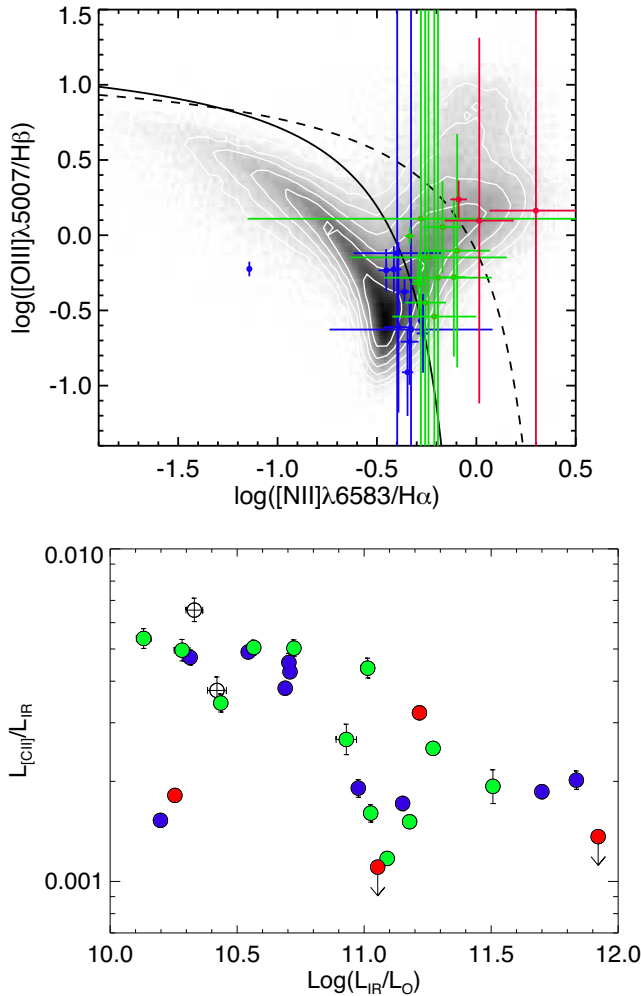
Figure 8. Top: the nature of our targets as shown by the BPT diagram (see Section 4.5). Nine galaxies present line ratios with large error bars (0.1 dex). Galaxies to the left of the solid line (taken from Kauffmann et al. 2003) are considered star forming (blue crosses); those to the right of the dashed line (taken from Kewley et al. 2001) are considered AGNs (red crosses); and those between the solid and dashed lines are defined as composites (green crosses). The background contours and grey-scale shows the distribution for the whole spectroscopic SDSS sample. Bottom: the [C II]/IR luminosity ratio as a function of IR luminosity, colour-coded by the BPT classification (same colours as above). The present data show that in this diagram the different populations are indistinguishable from each other.
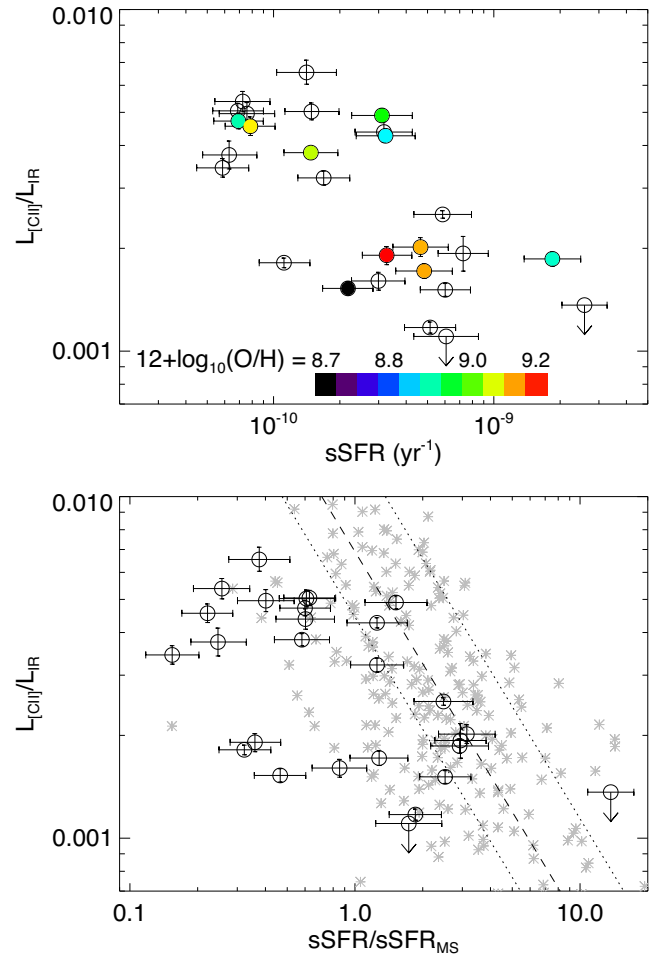
Figure 9. Top: the [C II]/IR luminosity ratio as a function of the sSFR, derived using the observed IR luminosity and stellar masses from SEDs fits to SDSS *ugriz* photometry (see Section 4.5 for details). Colour-coded we show metallicity measurements (using Tremonti et al. 2004's relation) for only those sources which are identified as star-forming in the BPT diagram (Fig. 8). Bottom: the same figure but dividing the sSFR values by the redshift dependent 'main-sequence' defined by Elbaz et al. (2011). In light grey asterisks, we show the galaxy sample presented by Díaz-Santos et al. (2013). The dashed line shows the correlation defined by Díaz-Santos et al. (see their equation 5 but converting $L_{IR} = 1.75 \times L_{FIR}$), including a ± 0.26 dex range of dispersion (dotted lines). Note how our sample is more representative of 'normal' galaxies (with respect to the 'main-sequence') compared to that presented by Díaz-Santos et al. (2013).

different and more inefficient star formation mechanism controlling the [C II]/IR ratio (Daddi et al. 2010; Graciá-Carpio et al. 2011).

5.1 The strength of the radiation field

Modelling the [C II] emission as coming from PDRs, we suggest that one of the main parameters responsible in controlling the [C II]/IR ratio is the strength of the far-UV radiation field ($\langle G_0 \rangle$). This is supported by the significant correlation found between dust temperatures, and Σ_{IR}, with the $L_{[C II]}/L_{IR}$ luminosity ratio. Higher dust temperatures suggest higher radiation fields generated by higher SFR surface densities, which might create large ionized complexes, especially expected in those galaxies with high IR luminosities $11 < \log_{10}(L_{IR}/L_\odot) < 12$. These more extreme conditions could

easily change the dominant ISM state responsible for the bulk of the [C II] emission (e.g. Díaz-Santos et al. 2013).

Actually, the far-UV radiation field (produced by O and B stars) is one of the main contributors to the heating of the gas via the photoelectric effect on dust grains. In the case of soft radiation fields, the ejection rate of photoelectrons from dust decreases (e.g. Spaans et al. 1994), while in the case of strong radiation fields, the dust grains become positively charged, increasing the potential well that the photoelectrons need to overcome, and thus reducing the input energy transferred to the gas by photoelectrons (Tielens & Hollenbach 1985; Malhotra et al. 1997, 2001; Luhman et al. 2003).

We suggest that the [C II]/IR ratio is controlled by the strength of the far-UV radiation fields, hence the decrement of the [C II] line with respect to IR emission is most probably due to an increment of positively charged dust grains (higher dust temperatures), which

reduces the efficiency of the far-UV radiation field in transferring energy into the gas.

Negishi et al. (2001) found that the $\langle G_O \rangle / n_e$ (where n_e is the density of electrons of the ISM) ratio does not drive the [C II]/IR ratio but they suggest that high gas densities play an important role in controlling the [C II] emission. Morphologically speaking, our analysis shows that galaxies with low [C II]/IR ratios tend to have prominent bulges in nuclear regions, i.e. probably suggesting that gas density plays an important role in the [C II]/IR ratio. However, we were unable to identify a clear correlation between [C II]/IR ratio and sSFR, indicating that more efficient SFR in compact regions is probably not controlling the [C II]/IR ratio (at least at the parameter space explored by this work). Unfortunately, with the available data presented in this work, we are unable to separate the intimate relation between the strength of the radiation field and the density of the ISM. To separate both parameters, we require [C II] together with another emission line, such as the fine transitions of [N II], [O I] and [C I] or rotational transitions of CO to properly determine the physical conditions of the ISM (e.g. Wolfire, Hollenbach & Tielens 1989; Hailey-Dunsheath et al. 2010).

5.2 The ISM origin of the [C II] emission

We show that galaxies presenting high [C II]/IR ratios have relatively cold dust temperatures, have dominant disc-like morphologies, and low surface brightness, evidences that indicate relatively weaker far-UV radiation fields. As previously shown by Pineda et al. (2014), the origin of the [C II] emission in the Milky Way (a 'normal' spiral galaxy) is not only from cold PDRs, but includes also contributions of the same order from ionized gas, diffuse atomic gas and CO-dark H_2. It is expected that weaker radiation fields would imply smaller complexes of ionized gas. We argue that sources with high [C II]/IR ratios might not only emit their [C II] luminosity from cold PDRs but also from the diffuse and extended atomic ISM phase. Without a H_2 tracer (e.g. CO lines), we are unable to prove this statement, although it points out to the difficulties in understanding the origin of the [C II] emission with a single far-IR line detection.

5.3 Old stellar populations contributing to the cold IR emission

The [C II] and IR luminosities are intimately related to the star formation process. In this section, we explore if the '[C II]-deficit' could be a manifestation of an inclusion of an IR emitting component which is not related to the star formation, but to old stellar populations. Actually, the IR SED component coming from dust heated by old stellar populations is cold, diffuse and is predominantly emitted at long $> 200\,\mu m$ wavelengths. We have explored the possibility that the 500 μm luminosity could correlate with the [C II]/IR ratio, although no clear trends are observed (see Table 2). If a prominent cirrus-like emission is present in these galaxies, the Rayleigh-Jeans would tend to have flatter spectra (between 250 and 500 μm), hence would tend to bias the fitted dust emissivity index (see also Appendix A) – this parameter basically controls the slope in the Rayleigh-Jeans regime. With the available data, it is not possible to distinguish different physical dust properties from a strong cirrus component. Nevertheless, it is worth mentioning that the anticorrelation found between best fit β and the [C II]/IR luminosity ratio (Fig. 5) suggests that it is unlikely that the bolometric IR luminosity is dominated by a cold cirrus component, hence responsible for the decrement seen in [C II]/IR as a function of IR luminosity.

This is in agreement with the selection criterion $S_{160\,\mu m} > 150\,\mathrm{mJy}$ which prefers galaxies dominated by star-forming heating.

5.4 Self-absorption or optically thick

Extraordinarily large column densities are required to make the [C II] emission optically thick. Self-absorption has been employed to explain the [C II] emission from AGN-dominated systems, like Mrk 231 (Fischer et al. 2010) where H I column densities could be higher than $10^{22}\,\mathrm{cm}^{-2}$. For most starburst galaxies this effect is expected to be small, especially at the luminosity range explored by this work $10 < \log_{10}(L_{IR}/L_\odot) < 12$. On the other hand, Gerin et al. (2015) have recently shown that on the plane of the Milky Way the presence of foreground absorption may completely cancel the emission from a background far-IR emitter in medium spectral resolution data, suggesting that spectra should be taken at high spectral resolution, e.g. using HIFI (de Graauw et al. 2010) rather than PACS, to interpret correctly the [C II] emission, therefore the [C II]/IR ratio.

In order to explore this idea, we have identified all four edge-on galaxies in our sample as possible optically thick [C II] candidates (along the line of sight). We find that all four galaxies are at the high end of the [C II]/IR luminosity ratio distribution. This result suggests that the [C II] emission might not be self-absorbed, at least by the disc, where most of the H II regions and surrounding PDRs are placed.

Supposing that the whole [C II] emission of the disc (mostly PDR-related) is absorbed, then the observed high [C II]/IR ratios should come from a diffuse [C II] component preferentially located above/below the disc. Note also that these edge-on galaxies tend to show line FWHMs which are $\gtrsim 200\,\mathrm{km\,s}^{-1}$ (see Table 3), helping the line emission to escape from the disc.

5.5 IR emission contaminated by an AGN

It has been previously shown that sources harbouring an AGN have lower [C II] to IR luminosity ratios (e.g. Sargsyan et al. 2012). In Fig. 8, we have classified star-forming galaxies from AGNs using the BPT diagram. Error bars are large, although we find that star-forming, composite and AGN populations are indistinguishable in terms of [C II]/IR luminosity ratios, possibly suggesting that the presence of an AGN might be playing a local but not a global role on the [C II]/IR luminosity ratios – at least at the low AGN luminosities presented in this work. This is supported by Díaz-Santos et al. (2013) as they found that AGNs selected by a simple PAH equivalent width threshold do not modify significantly the [C II]/IR luminosity ratio.

6 CONCLUSION

We have used recent PACS spectroscopic [C II] observations to describe its relation to the IR luminosity in a sample of 28 galaxies selected from the *H*-ATLAS survey. This sample has high-quality IR photometry from *WISE*, *IRAS* and *Herschel*, with the addition of unambiguous photometry and spectroscopy from the SDSS and GAMA surveys.

In summary, after an exploration over a wide multiwavelength parameter space, we have identified the following correlations. We find that galaxies with high $L_{[CII]}/L_{IR} > 2.5 \times 10^{-3}$ luminosity ratios tend to: have $L_{IR} < 10^{11}\,L_\odot$, dust temperatures lower than 30 K, high *WISE* colours in the range $0.5 < S_{12\,\mu m}/S_{22\,\mu m} < 1.0$, present disc-like morphologies, have low surface brightness

$\Sigma_{IR} \approx 10^{8-9}\,L_\odot/kpc^2$ (using the *r*-band effective radius), and got a range of SFR efficiencies (sSFR ≈ 0.05–$3\,Gyr^{-1}$).

Assuming that the physical properties of star-forming galaxies, at fixed luminosity, are the same at $z = 0.02$ and 0.2 (the range of redshift of our galaxy sample), and based on the correlations found between the [C II]/IR luminosity ratio and the dust temperature (and Σ_{IR}), we conclude that the most probable parameter controlling the [C II]/IR luminosity ratio is the strength of the radiation field (averaged over the entire galaxy) – probably inducing an increment of the positive charge of dust grains that has an effect in the effective energy deposited by the radiation field in the electrons extracted from dust grains.

The lack of correlation between galaxies with high [C II]/IR luminosity ratios ($>3 \times 10^{-3}$) and sSFR values suggests that the efficiency to convert gas into stars (e.g. in high-density environments) is not playing a dominant role in the line to continuum behaviour, contrary to the correlation found by Díaz-Santos et al. (2013). We are probably observing a plateau for the correlation at lower SFR/SFR$_{MS}$ < 1 ratios, maybe product of a different star-forming mechanism that controls the [C II]/IR ratio.

We find that the [C II] deficit is unlikely to be a manifestation of optically thick [C II] emission, as evidenced by the high [C II]/IR luminosity ratios found in edge-on spiral galaxies. On the other hand, the analysis we performed to characterize the nature of our galaxies, using the BPT diagram, is not conclusive as all star-forming galaxies, AGNs and composite populations do not clearly distinguish from each other in terms of the [C II]/IR luminosity ratio. We conclude that at least at the AGN luminosities shown by our sample, AGN activity does not seem to play a dominant role in the [C II] deficit.

ACKNOWLEDGEMENTS

REFERENCES

Abel N. P., Dudley C., Fischer J., Satyapal S., van Hoof P. A. M., 2009, ApJ, 701, 1147
Adelman-McCarthy J. K. et al., 2008, ApJS, 175, 297
Bakes E. L. O., Tielens A. G. G. M., 1994, ApJ, 427, 822
Baldwin J. A., Phillips M. M., Terlevich R., 1981, PASP, 93, 5
Boreiko R. T., Betz A. L., 1995, ApJ, 454, 307
Bruzual G., Charlot S., 2003, MNRAS, 344, 1000
Calzetti D., Armus L., Bohlin R. C., Kinney A. L., Koornneef J., Storchi-Bergmann T., 2000, ApJ, 533, 682
Chabrier G., 2003, PASP, 115, 763
Contursi A. et al., 2002, AJ, 124, 751
Cormier D. et al., 2012, A&A, 548, A20
Curran S. J., 2009, A&A, 497, 351
Daddi E. et al., 2010, ApJ, 714, L118
Dalgarno A., McCray R. A., 1972, ARA&A, 10, 375
De Breuck C., Maiolino R., Caselli P., Coppin K., Hailey-Dunsheath S., Nagao T., 2011, A&A, 530, L8
De Breuck C. et al., 2014, A&A, 565, 59
de Graauw T. et al., 2010, A&A, 518, L6
De Looze I. et al., 2014, A&A, 568, A62
Díaz-Santos T. et al., 2013, ApJ, 774, 68
Driver S. P. et al., 2009, Astron. Geophys., 50, 050000
Driver S. P. et al., 2011, MNRAS, 413, 971
Dunne L. et al., 2011, MNRAS, 417, 1510
Eales S. et al., 2010, PASP, 122, 499
Elbaz D. et al., 2011, A&A, 533, A119
Farrah D. et al., 2013, ApJ, 776, 38
Fischer J. et al., 2010, A&A, 518, L41
Genzel R. et al., 2010, MNRAS, 407, 2091
George R. D. et al., 2013, MNRAS, 436, L99
Gerin M. et al., 2015, A&A, 573, A30
Graciá-Carpio J. et al., 2011, ApJ, 728, L7
Griffin M. J. et al., 2010, A&A, 518, L3
Hailey-Dunsheath S., Nikola T., Stacey G. J., Oberst T. E., Parshley S. C., Benford D. J., Staguhn J. G., Tucker C. E., 2010, ApJ, 714, L162
Herrera-Camus R. et al., 2015, ApJ, 800, 1
Hill D. T. et al., 2011, MNRAS, 412, 765
Hopkins A. M. et al., 2013, MNRAS, 430, 2047
Ibar E. et al., 2010, MNRAS, 409, 38
Ibar E. et al., 2013, MNRAS, 434, 3218
Ivison R. J. et al., 2010, A&A, 518, L35
Kauffmann G. et al., 2003, MNRAS, 346, 1055
Kelvin L. S. et al., 2012, MNRAS, 421, 1007
Kennicutt R. C., Jr, 1998, ARA&A, 36, 189
Kewley L. J., Dopita M. A., Sutherland R. S., Heisler C. A., Trevena J., 2001, ApJ, 556, 121
Kramer C. et al., 2013, A&A, 553, A114
Kroupa P., Weidner C., 2003, ApJ, 598, 1076
Lara-López M. A., Cepa J., Bongiovanni A., Pérez García A. M., Castañeda H., Fernández Lorenzo M., Pović M., Sánchez-Portal M., 2009, A&A, 505, 529
Lara-López M. A. et al., 2013, MNRAS, 434, 451
Luhman M. L., Satyapal S., Fischer J., Wolfire M. G., Sturm E., Dudley C. C., Lutz D., Genzel R., 2003, ApJ, 594, 758
Madden S. C., 2000, New Astron. Rev., 44, 249
Madden S. C., Geis N., Genzel R., Herrmann F., Jackson J., Poglitsch A., Stacey G. J., Townes C. H., 1993, ApJ, 407, 579
Maiolino R. et al., 2005, A&A, 440, L51
Maiolino R., Caselli P., Nagao T., Walmsley M., De Breuck C., Meneghetti M., 2009, A&A, 500, L1
Malhotra S. et al., 1997, ApJ, 491, L27
Malhotra S. et al., 2001, ApJ, 561, 766
Nakagawa T., Matsuhara H., Kawakatsu Y., 2012, in Clampin M. C., Fazio G. G., MacEwen H. A., Oschmann J. M., Jr, eds, Proc. SPIE Conf. Ser. Vol. 8442, Space Telescopes and Instrumentation 2012: Optical, Infrared, and Millimeter Wave. SPIE, Bellingham, p. 84420O

Negishi T., Onaka T., Chan K.-W., Roellig T. L., 2001, A&A, 375, 566

Pascale E. et al., 2011, MNRAS, 415, 911

Pettini M., Pagel B. E. J., 2004, MNRAS, 348, L59

Pilbratt G. L. et al., 2010, A&A, 518, L1

Pineda J. L., Langer W. D., Velusamy T., Goldsmith P. F., 2013, A&A, 554, A103

Pineda J. L., Langer W. D., Goldsmith P. F., 2014, A&A, 570, 121

Poglitsch A. et al., 2010, A&A, 518, L2

Polletta M. et al., 2007, ApJ, 663, 81

Riechers D. A. et al., 2013, Nature, 496, 329

Riechers D. A. et al., 2014, ApJ, 796, 84

Rigby E. E. et al., 2011, MNRAS, 415, 2336

Rowan-Robinson M. et al., 2010, MNRAS, 409, 2

Rubin D. et al., 2009, A&A, 494, 647

Sanders D. B., Mirabel I. F., 1996, ARA&A, 34, 749

Sargsyan L. et al., 2012, ApJ, 755, 171

Seki J., Yamamoto T., 1980, Ap&SS, 72, 79

Shetty R., Kauffmann J., Schnee S., Goodman A. A., 2009, ApJ, 696, 676

Smith D. J. B. et al., 2011, MNRAS, 416, 857

Smith D. J. B. et al., 2013, MNRAS, 436, 2435

Solomon P. M., Vanden Bout P. A., 2005, ARA&A, 43, 677

Spaans M., Tielens A. G. G. M., van Dishoeck E. F., Bakes E. L. O., 1994, ApJ, 437, 270

Stacey G. J., Geis N., Genzel R., Lugten J. B., Poglitsch A., Sternberg A., Townes C. H., 1991, ApJ, 373, 423

Stacey G. J., Hailey-Dunsheath S., Ferkinhoff C., Nikola T., Parshley S. C., Benford D. J., Staguhn J. G., Fiolet N., 2010, ApJ, 724, 957

Swinbank A. M. et al., 2012, MNRAS, 427, 1066

Taylor M. B., 2005, in Shopbell P., Britton M., Ebert R., eds, ASP Conf. Ser. Vol. 347, Astronomical Data Analysis Software and Systems XIV. Astron. Soc. Pac., San Francisco, p. 29

Taylor E. N. et al., 2011, MNRAS, 418, 1587

Tielens A. G. G. M., Hollenbach D., 1985, ApJ, 291, 722

Tremonti C. A. et al., 2004, ApJ, 613, 898

Valtchanov I. et al., 2011, MNRAS, 415, 3473

Walter F., Riechers D., Cox P., Neri R., Carilli C., Bertoldi F., Weiss A., Maiolino R., 2009, Nature, 457, 699

Wang L., Rowan-Robinson M., Norberg P., Heinis S., Han J., 2014, MNRAS, 442, 2739

Wolfire M. G., Hollenbach D., Tielens A. G. G. M., 1989, ApJ, 344, 770

Wolfire M. G., Tielens A. G. G. M., Hollenbach D., 1990, ApJ, 358, 116

Wright E. L. et al., 2010, AJ, 140, 1868

Young J. S., Schloerb F. P., Kenney J. D., Lord S. D., 1986, ApJ, 304, 443

APPENDIX A: TESTING FITTED PARAMETERS

As described in Section 4, our SED fitting approach includes a non-standard method. The inclusion of the power law in the mid-IR forces the slope of the MBB emission at ∼100–200 μm, possibly introducing a bias on the derived dust temperature or dust emissivity index. For this reason, we repeated the SED fitting approach excluding the mid-IR slope, leaving just the MBB (from equation 2) component. For these purposes, we just use the *Herschel* photometry, i.e. the 100, 160, 250, 350 and 500 μm data points. We also restricted, between 1.5 and 2.5, the range of possible values for the dust emissivity index.

The first thing to note is that these new fits are unable to describe the high-frequency part of the spectra, hence we cannot use them to get bolometric IR measurements. These new fits, however, show a clear difference between derived parameters. On average, we find that with this new SED-fitting method, the T_{dust} decreased by ∼6 K while β increased by ∼0.5 – parameters which are well known to be correlated (e.g. Shetty et al. 2009; Smith et al. 2013). These results are shown in Fig. A1. This clearly demonstrate that converting from
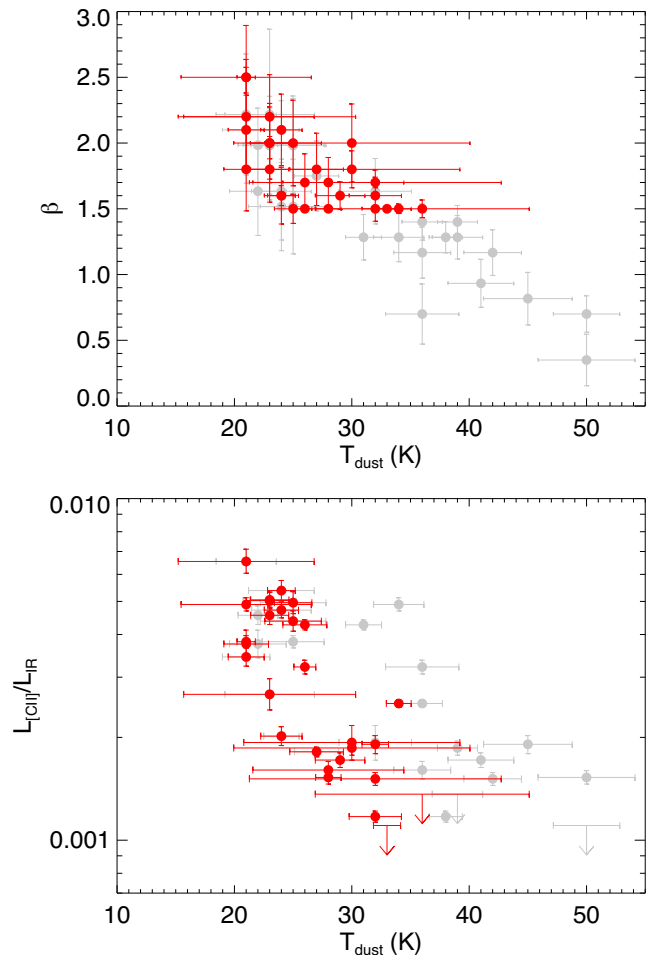

Figure A1. Top: a comparison between derived parameters, T_{dust} and β, using two different SED fitting approaches. In grey, we show the values obtained following the method described in Section 4. In red, we present the values obtained by fitting a MBB emission using only the *Herschel* 100–500 μm photometry (as usually performed in previous *Herschel*-based studies). Bottom: the [C II]/IR luminosity ratio as a function of fitted dust temperature. Colours are the same as in the top figure. This comparison shows that the dependence for [C II]/IR as a function of T_{dust} (seen in Fig. 5) remains with this different SED-fitting approach.

fitted parameters to 'physical' parameters should be taken with great caution.

Even though a significant difference is seen between derived parameters coming from these two different SED fitting approaches, the previous trend seen in [C II]/IR luminosity ratio as a function of dust temperature remains (see Fig. A1). This confirms, again, that high [C II]/IR ratios are associated with galaxies dominated by cold dust emission.

[1]*Instituto de Física y Astronomía, Universidad de Valparaíso, Avda. Gran Bretaña 1111, Valparaiso, Chile*

[2]*Instituto de Astronomía, Universidad Nacional Autónoma de México, A.P. 70-264, 04510 México, D.F., México*

[3]*Australian Astronomical Observatory, PO Box 915, North Ryde, NSW 1670, Australia*

[4]*Department of Astronomy, University of Maryland, College Park, MD 20742-2421, USA*

[5]*Astrophysics Group, Imperial College London, Blackett Laboratory, Prince Consort Road, London SW7 2AZ, UK*

[6]*European Southern Observatory, Karl-Schwarzschild-Straße 2, D-85748 Garching bei München, Germany*

[7]*Institute for Astronomy, University of Edinburgh, Royal Observatory, Blackford Hill, Edinburgh EH9 3HJ, UK*

[8]*Universität Wien, Institut für Astrophysik, Türkenschanzstraße 17, A-1180 Vienna, Austria*

[9]*Leiden Observatory, Leiden University, PO Box 9513, NL-2300 RA Leiden, the Netherlands*

[10]*California Institute of Technology, 1200 E. California Blvd, Pasadena, CA 91125, USA*

[11]*Department of Astronomy, Cornell University, 220 Space Sciences Building, Ithaca, NY 14853, USA*

[12]*Sterrenkundig Observatorium, Universiteit Gent, Krijgslaan 281 S9, B-9000 Gent, Belgium*

[13]*Herschel Science Centre, European Space Astronomy Centre, Villanueva de la Cañada, E-28691 Madrid, Spain*

[14]*Department of Physics and Astronomy, University of Canterbury, Private Bag 4800, Christchurch 8140, New Zealand*

[15]*Department of Astrophysics, Denys Wilkinson Building, University of Oxford, Keble Road, Oxford OX1 3RH, UK*

[16]*Department of Physics & Astronomy, University of California, Irvine, CA 92697, USA*

[17]*INAF - Osservatorio Astronomico di Padova, Vicolo dell'Osservatorio 5, I-35122 Padova, Italy.*

[18]*SISSA, Via Bonomea 265, I-34136 Trieste, Italy*

[19]*School of Physics and Astronomy, University of Nottingham NG7 2RD, UK*

[20]*School of Physics and Astronomy, Cardiff University, Queens Buildings, The Parade, Cardiff CF24 3AA, UK*

[21]*CAPES Foundation, Ministry of Education of Brazil, Brasilia/DF 70040-020, Brazil*

[22]*Institute of Cosmology and Gravitation, University of Portsmouth, Dennis Sciama Building, Burnaby Road, Portsmouth PO1 3FX, UK*

This paper has been typeset from a TEX/LATEX file prepared by the author.